



**HAL**  
open science

## Monitoring of SAGD Process: Seismic Interpretation of Ray+Born Synthetic 4D Data

Caroline Joseph, Gisèle Etienne, Eric Forgues, Axelle Baroni, Gérard Renard,  
Eric Bathellier

► **To cite this version:**

Caroline Joseph, Gisèle Etienne, Eric Forgues, Axelle Baroni, Gérard Renard, et al.. Monitoring of SAGD Process: Seismic Interpretation of Ray+Born Synthetic 4D Data. Oil & Gas Science and Technology - Revue d'IFP Energies nouvelles, 2012, 67 (2), pp.263-288. 10.2516/ogst/2011168 . hal-00735134

**HAL Id: hal-00735134**

**<https://ifp.hal.science/hal-00735134>**

Submitted on 25 Sep 2012

**HAL** is a multi-disciplinary open access archive for the deposit and dissemination of scientific research documents, whether they are published or not. The documents may come from teaching and research institutions in France or abroad, or from public or private research centers.

L'archive ouverte pluridisciplinaire **HAL**, est destinée au dépôt et à la diffusion de documents scientifiques de niveau recherche, publiés ou non, émanant des établissements d'enseignement et de recherche français ou étrangers, des laboratoires publics ou privés.

# Monitoring of SAGD Process: Seismic Interpretation of Ray+Born Synthetic 4D Data

C. Joseph<sup>1</sup>, G. Etienne<sup>1</sup>, E. Forgues<sup>2</sup>, O. Lerat<sup>1</sup>, A. Baroni<sup>1</sup>, G. Renard<sup>1</sup> and E. Bathellier<sup>2</sup>

<sup>1</sup> IFP Energies nouvelles, 1-4 avenue de Bois-Préau, 92852 Rueil-Malmaison Cedex - France

<sup>2</sup> CGGVeritas, 27 avenue Carnot, 91341 Massy Cedex - France

e-mail: caroline.joseph@ifpen.fr - gisele.etienne@ifpen.fr - eric.forgues@cggveritas.com - olivier.lerat@ifpen.fr - axelle.baroni@ifpen.fr  
gerard.renard@ifpen.fr - eric.bathellier@cggveritas.com

**Résumé — Monitoring de procédé SAGD : interprétation sismique de données 4D synthétiques ray+Born** — L'objectif de cette étude est d'évaluer quelle information de production peut être déduite d'une campagne sismique 4D durant le procédé de récupération par injection de vapeur SAGD (*Steam-Assisted Gravity Drainage*). En plus des hétérogénéités réservoir d'origine géologique, de nombreux facteurs interagissent pendant la production thermique d'huile lourde et de bitume, ce qui complique l'interprétation des données sismiques 4D : variation de la viscosité de l'huile, des saturations en fluide, de la pression de pore, etc.

Cette étude est basée sur le champ pétrolier Hangingstone de la formation McMurray en Athabasca (Canada). Dans des travaux antérieurs, un modèle statique initial (géologique, pétroacoustique et géomécanique) avait été construit. Puis la production thermique d'huile lourde avait été simulée en mettant en œuvre le couplage d'un modèle d'écoulement de réservoir et d'un modèle géomécanique. Les paramètres sismiques des roches saturées (densité, vitesses de compression et de cisaillement) avaient alors été calculés à plusieurs étapes de la production à partir des paramètres mécaniques et de réservoir.

À partir de ces résultats, une acquisition sismique est simulée à quatre états de production SAGD. Comme on s'intéresse aux réflexions sismiques en ondes de compression générées dans le réservoir, une modélisation sismique orientée cible est choisie. Cette modélisation est basée sur une approche ray+Born et permet de calculer la réponse sismique en estimant correctement les amplitudes sismiques en fonction de l'offset (distance source-récepteur). Pour obtenir des données plus réalistes, du bruit réel incohérent est ajouté aux données sismiques synthétiques.

Les jeux de données synthétiques non bruitées et bruitées sont ensuite traités afin d'obtenir des images sismiques temps sommées et migrées. Une séquence simple de traitement sismique permet d'imager le développement de la chambre de vapeur, en particulier sa forme en V dans le plan perpendiculaire aux drains horizontaux, et d'observer des différences de temps de trajet dans la zone réservoir.

Un travail d'interprétation est alors mené sur ces données sismiques synthétiques à différents états de production. Plusieurs attributs sismiques, comme les valeurs RMS des variations d'amplitude entre états, les variations de temps de trajet à la base du réservoir entre états, ou l'énergie des images sismiques à chaque état, sont calculés sur les données synthétiques non bruitées et bruitées. Quelques attributs sismiques apparaissent robustes au bruit et impactés par la production. Les relations entre ces attributs sismiques et les propriétés réservoir/géomécaniques (lithofaciès, pression, température, saturation en vapeur d'eau, etc.) sont aussi évaluées. Enfin, concernant l'interprétation sismique, des corps réservoir connectés (*geobodies*) sont extraits des attributs sismiques.

**Abstract – Monitoring of SAGD Process: Seismic Interpretation of Ray+Born Synthetic 4D Data** – The objective of this study is to evaluate which production information can be deduced from a 4D seismic survey during the Steam-Assisted Gravity Drainage (SAGD) recovery process. Superimposed on

*reservoir heterogeneities of geological origin, many factors interact during thermal production of heavy oil and bitumen reservoirs, which complicate the interpretation of 4D seismic data: changes in oil viscosity, in fluid saturations, in pore pressure and so on.*

*This study is based on the real Hangingstone field case of the McMurray formation in the Athabasca region (Canada). In previous works, an initial static model (geology, petroacoustic and geomechanical) has been constructed and a thermal production of heavy oil with two coupled fluid-flow and geomechanical models has been simulated. Seismic parameters (density, compression velocity and shear velocity) of the saturated rocks have then been computed from mechanical and reservoir parameters at several stages of the production.*

*A repeated acquisition survey is modelled at different stages of SAGD production. This is performed using a 3D seismic modelling approach. To focus on the reflections generated within the reservoir zone, a target-oriented modelling is chosen. It is based on the ray+Born approach which permits to compute the P-wave elastic response by correctly handling the seismic amplitudes as a function of source-receiver offset. Real incoherent noise is added to the zero-phase synthetic data to produce a more realistic result. The noise-free and the noisy synthetic data are processed to get stacked and time migrated images. A simple processing workflow leads to image the steam chamber development, in particular its V-shape in radial section, and to observe time-lapse in the reservoir zone.*

*An interpretation work is then carried out. Some seismic attributes like RMS values of amplitude changes between stages, energy, time differences of reservoir bottom between stages, etc. are computed from the synthetic (noise-free and noisy) seismic data. Some of these attributes prove to be robust to the noise and to show some production effect. Possible trends between these attributes and the modelled reservoir/geomechanical properties (lithofacies, pressure, temperature, steam saturation, etc.) are also evaluated. Finally, geobodies are extracted from the seismic attributes.*

## INTRODUCTION

The performance of heavy oil production by Steam-Assisted Gravity Drainage (SAGD) recovery process is affected by reservoir heterogeneities. Pressure and temperature variations during thermal production operations induce stress changes in the reservoir and in the surrounding media. These modifications of the stress state may imply deformations that can, in turn, have an impact on reservoir production. These changes have therefore an influence on both densities and seismic velocities, consequently on the wave propagation into rocks and fluids along production and 4D seismic data. On such heavy oil reservoirs produced by SAGD, the literature shows that associated 4D seismic data are analyzed either in a qualitative way [1, 2], or in a more precise/quantitative way by using PetroElastic or Rock Physics Modelling [3-5]. Moreover, additional information of higher frequency content than traditional seismic has proven to be of great help for understanding the reservoir heterogeneities and production problems (e.g. [6], combining standard and crosswell seismic over 500 Hz).

For this study, a model representative of an Athabasca heavy oil unconsolidated sands reservoir was constructed [7]. First, the initial static model was constructed with a geostatistical approach, considering five lithofacies for the reservoir (three sandstones from coarse to fine-grained, and two shaly facies) and three lithofacies (from sands to shales) for the overburden up to the surface. Second, the thermal production of heavy oil was then simulated along calendar time with two

coupled fluid-flow and geomechanical models. The use of a negative thermal expansion coefficient for the shales allowed the possible collapse of the shale materials and thus a potential pass through for the steam. Elastic models were then generated along calendar time: the elastic parameters were carefully estimated according to the oil viscosity (temperature and pressure dependent), the oil and water saturations and the geomechanical effect through a stress Hertz coefficient.

Four production stages are considered here: the initial stage before steam injection, and the stages of 1st month of production, 6th month of production, and 3rd year of production.

The 4D seismic modelling mimics a permanent surface acquisition survey. To focus on the reflections generated within the reservoir zone, a 3D target-oriented modelling tool is chosen. This tool is based on the ray+Born formalism [8-10] which allows us to compute the P-wave elastic response, by correctly handling the seismic amplitudes as a function of source-receiver offset. In particular, the effects of the overburden and of the survey are taken into account. Some real noise is then added to the computed seismic data.

Based on these 4D stacked synthetic seismic data, an interpretation is carried out to answer these points:

- first, better understand the evolution of the 4D seismic amplitudes as a function of calendar time in terms of production (pressure, temperature and fluid saturations) and mechanical effects (stress and strain);
- second, provide guidelines for the interpretation of real 4D seismic data;

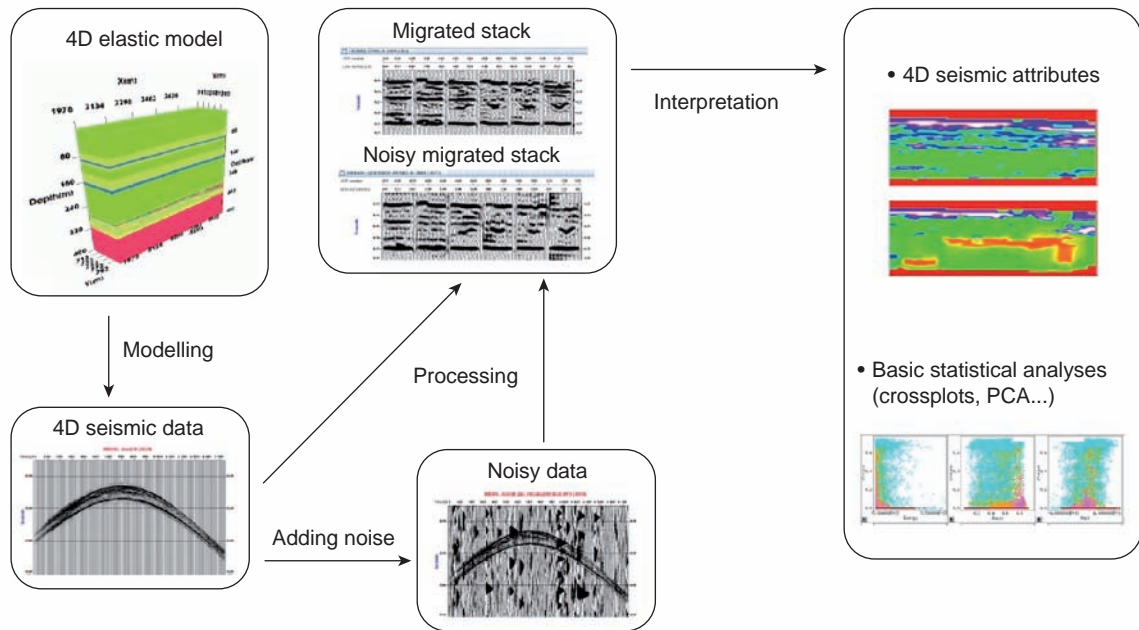


Figure 1

General scope of the seismic modelling and interpretation study.

- third, assess the interest of permanent acquisition technology in heavy oil reservoirs produced by SAGD.

In this paper, we first briefly summarize these early works on model building and steam injection/production, then we present our results on 4D seismic modelling and interpretation related to some seismic attributes and their link with the reservoir/geomechanical properties (qualitative or quantitative), as well as geobody computations (see *Fig. 1* for the general scope).

## 1 A REALISTIC MODEL OF A SAGD WELL PAIR [7]

The model represents the Hangingstone field located in Northern Alberta (Canada) in the Athabasca oil sands province. The reservoirs are made of unconsolidated sands from the fluvio-estuarine McMurray Formation (Mannville Group, Lower Cretaceous). Reservoirs from this area exhibit a complex internal architecture which is associated with heterogeneities (shales) specific to fluvial and estuarine environments. The heavy oil reservoir is at a relatively shallow depth of 260 m in average. Its thickness is close to 50 m.

The simulation of thermal production of heavy oil in the reservoir is fully described in [7]. The approach is based on a fluid-flow model explicitly coupled with a geomechanical one.

The main steps of the simulation workflow are summarized below.

### 1.1 Geological Model

A 3D detailed geological model of the reservoir has been constructed on a very fine grid by a geostatistical approach, constrained by both horizontal and vertical wells (*Fig. 2*):

- first, the geological model was defined at a very fine scale near the well bores in order to preserve the description of heterogeneities (shales);
- second, it was populated with lithofacies (*see Tab. 1*) and two initial petrophysical properties (porosity and permeability).

The overburden up to the surface was modelled on a much coarser grid in the vertical direction (with sandstones, shales and sands, shales lithofacies).

Finally, a SAGD well pair was extracted from the whole model.

TABLE 1  
Description of the lithofacies at the reservoir level

Name	Material	Color-code
Lithofacies 1	Clean medium to coarse-grained sandstone facies	
Lithofacies 2	Clean medium-grained sandstone facies	
Lithofacies 3	Fine-grained sandstone facies	
Lithofacies 4	Silty shales facies	
Lithofacies 5	Shales	

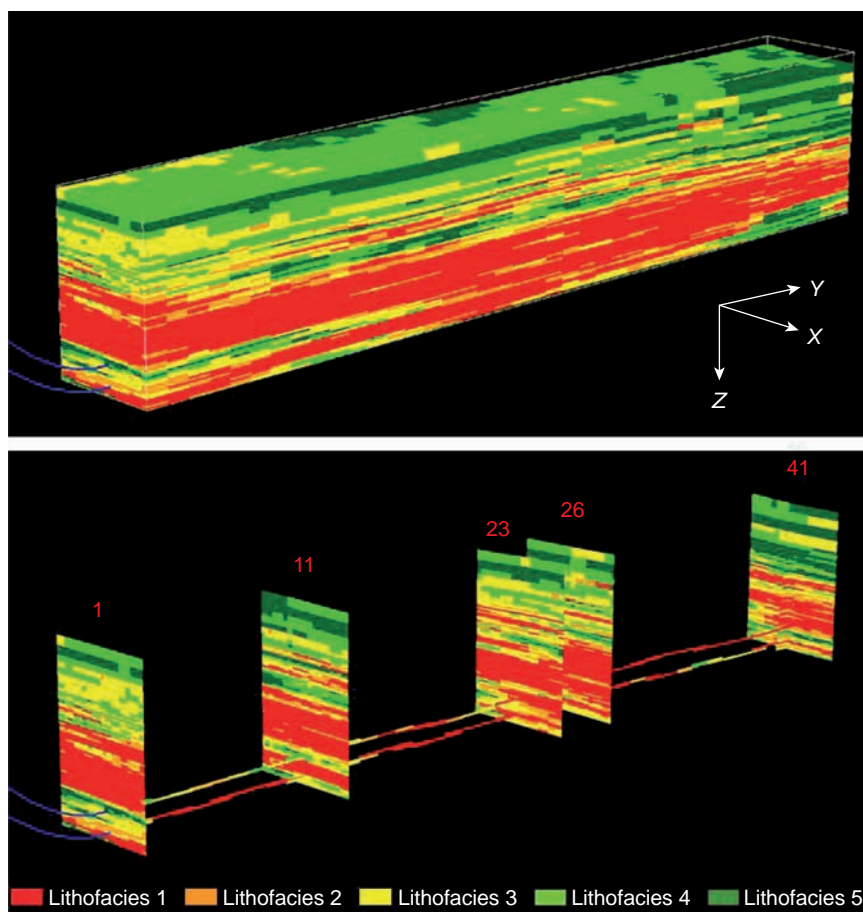


Figure 2

Distribution of heterogeneities in the reservoir (top) and on selected sections and along SAGD well pair (bottom). See Table 1 for lithofacies description. Reservoir cube of 100 m wide ( $X$ ), 820 m long ( $Y$ ), 50 m high ( $Z$ ).

## 1.2 Reservoir/Geomechanical Model

This fine-scale geological model was then used to build a mechanical model in the reservoir part. Poro-elastic properties were assigned to the cells according to the lithofacies and associated porosity. This assignment was based on a consistent interpretation and integration of available log data and core data. At a temperature of 10°C, the oil viscosity is about 2 000 000 cP and its density is about 8°API. Production data available for this study consisted of steam injection and oil production rates.

A simulation was performed for a selection of time periods of steam injection on the SAGD well pair, with a fluid-flow model coupled with a geomechanical one. The modelling focused on the first six months of production and on a later period comprised between one and three years. An explicit coupling scheme was performed with an update of the reservoir permeabilities at chosen steps of simulation. The reservoir

simulation results are in good agreement with field data. Figure 3 presents the simulated extension of the steam chamber after six months and three years of production. The 3D envelope corresponds to a minimum temperature of 100°C, which means that every cell inside the envelope has a temperature ranging between 100°C-280°C (maximum temperature observed in the reservoir during production). This figure shows a high degree of heterogeneity of temperature distribution along the well pair, especially for short durations. Indeed, after six months the steam chamber development seems to be confined vertically from sections 1 to 11. These sections coincide with the presence of heterogeneities (shales) at the heel of the well (*see Fig. 2*).

## 1.3 4D Elastic Model

Because there are three main sources of stress dependency of wave velocities (changes in porosity with stress, existence of



Figure 3

Steam chamber extent corresponding to temperatures over 100°C after six months (left) and three years (right) of production.

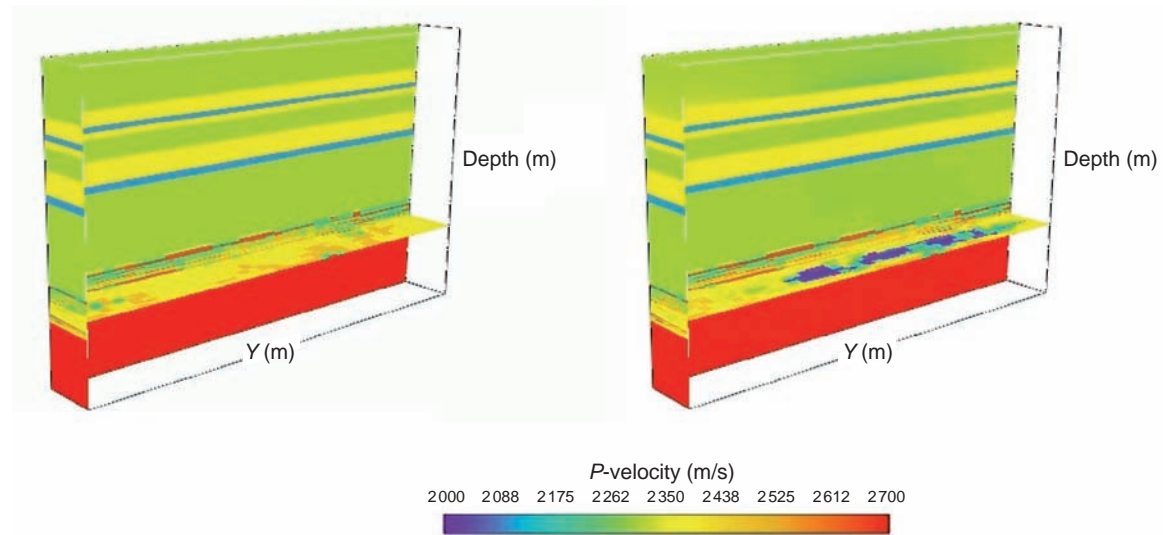


Figure 4

$P$ -velocity model (100 m wide, 820 m long, 400 m high): initial stage (left), 3rd year of production (right).

grain contacts and presence of cracks) a stress-sensitive rock-physics model was required. The Hertz-Mindlin's contact theory was used as a first approach. This model is based on the evolution of the contact surface between two spherical particles and accounts for the impact of mean effective stresses on both  $P$ - and  $S$ -wave velocities. As the impact of temperature on these velocities is not well established, a simple model issued from literature was used. The effects of fluid saturations on effective bulk modulus, then on velocities, were inferred from Biot-Gassmann theory.

The initial seismic parameters (density, compression velocity and shear velocity) of the saturated rocks were estimated from initial mechanical and reservoir parameters in coherence with the well log data. Before the warm-up phase, only water and oil components are present in our fluid model, but heavy oil has been considered almost a solid due to its high viscosity. Therefore the generalized Gassmann's equations [11] were handled under the simplifications of a homogeneous grain rock and of a uniform macroscopic fluids repartition.

Another challenge was that the determination of seismic parameters requires dynamic mechanical parameters (Young's modulus, Poisson's ratio), whereas mechanical parameters used in mechanical modelling are static.

Each material was assigned the elastic properties corresponding to the initial water saturation set to 0.15 in the reservoir sands materials, and set to 1 in all other materials, as observed from well logs. The 3D full model was then populated with density,  $P$ - and  $S$ -velocities (Fig. 4). In the overburden, the  $P$ - to  $S$ -velocities ratio is in a 2.5 to 3.1 range, whereas in the reservoir it falls between 2.0 and 3.0.

Concerning the 4D model, the basic idea was that the seismic properties of the oil saturated rocks are related to seismic properties of heavy oils which depend on density, composition, temperature and gas/oil ratio.

The evolution of physical parameters during steam injection was computed thanks to the coupling of the reservoir and geomechanical models. These changes were used

to dynamically update the seismic velocities both in the overburden and in the reservoir:

- temperature, saturation and pore pressure evolutions, computed by the fluid flow simulation, were taken into account in the reservoir only;
- stress and strain evolutions, computed by the geomechanical simulation, were taken into account in both the reservoir and the overburden regions.

The evolution of these physical parameters drives the modification of mechanical parameters (dry modulus, fluid modulus and density) which pilot saturated modulus. The evolution of both saturated modulus and density pilots wave velocity changes.  $P$ - and  $S$ -velocities decrease inside the slim core of the steam chamber associated with the presence of gaseous water and in heated-up shales (elsewhere it depends).

## 2 4D SYNTHETIC PERMANENT ACQUISITION SURVEY

### 2.1 Seismic Modelling

#### 2.1.1 Ray+Born Modelling

Our objective is to compute the wave reflections occurring in an elastic target zone. We consider a 3D seismic modelling based on the ray+Born formalism [12] which corresponds to a linearization of the wave equation around a reference medium. On the one hand, the wave propagation between the surface and the target is simulated with the help of a 3D ray-tracing in the reference medium. On the other hand, the modelling of the reflections/diffractions in the target is performed with the help of amplitude computing using the Born approximation [13].

The ray+Born technique allows us to compute the elastic response, by correctly handling the seismic amplitudes as a function of source-receiver offset. In particular, the effect of the overburden and survey is included. The multiple reflections and refractions are not modelled. The main advantage of this method is that the simulation is fast computing; and the main disadvantage is that the modelling is not suitable for models with strong velocity variations.

The Born approximation decomposes the model  $m$  into the sum of a reference medium  $m_0$  and a perturbation target  $\delta m$ . The reference medium  $m_0$  corresponds to the large spatial wavelengths of the model and governs the wave propagation in terms of traveltime, geometrical spreading and wave front directivity. We call Green's function the seismic response of a unitary point computed in the reference medium for an impulse source. The perturbation target  $\delta m$  corresponds to the small spatial wavelengths of the model and influences the wave reflection and diffraction amplitudes. The Born approximation is valid for relative

perturbations of low amplitude and of small size compared with the wavelength of the wavefield. More precisely, the validity condition may be written as [14]:

$$\frac{\delta p}{p_0} \frac{2\pi}{\lambda} R \ll 1$$

where  $\lambda$  is the wavelength of the wavefield,  $R$  is the significant size of perturbation elements and  $\delta p/p_0$  is the average value of perturbation parameters. In the case of a very small significant size of perturbation elements, the average value of perturbation parameters can be not very weak such as a value of 0.1. This statement has been confirmed by many studies on different types of elastic model [15, 16].

We used an in-house software for computing the  $P$ -wave elastic response. The ray-tracing is performed in the smooth reference medium  $m_0$ : traveltimes, ray amplitudes and slowness vectors are delivered. These quantities of incident and diffracted rays make up the Green's functions (one for each couple source-target point and each couple receiver-target point).

For one source  $s$ , a seismic trace  $U$  is associated with each receiver  $r$  and corresponds to the displacement vector in function of time  $t$ . We note  $T$  the traveltime,  $Ampli_{3D}$  the ray amplitude and  $S(t)$  the emitted wavelet. The perturbation  $\delta m/m_0$  is represented by relative perturbations in  $P$ -impedance  $\delta Ip/Ip_0$ , in  $S$ -impedance  $\delta Is/Is_0$  and in density  $\delta\rho/\rho_0$  where the subscript 0 refers to the reference medium. Each trace  $U$  associated with a couple  $(s,r)$  is composed of the contributions of each point  $x_\Omega$  of the target  $\Omega$ :

$$U(s,r,t) = -\frac{\partial S(t)}{\partial t^2} * \int_{\Omega} Ampli_{3D}(s,x_\Omega,r) Diffraction(s,x_\Omega,r) \delta(t-T(s,x_\Omega,r)) dx_\Omega$$

where  $*$  denotes the convolution operator and  $\delta$  denotes the Dirac function. The term *Diffraction* is expressed as:

$$Diffraction(s,r,x_\Omega) = [\cos\theta - (1 - 2\gamma_0^2) - 2\gamma_0^2 \cos^2\theta] \frac{\delta\rho}{\rho_0}(x_\Omega) + 2 \frac{\delta Ip}{Ip_0}(x_\Omega) + 4\gamma_0^2(\cos^2\theta - 1) \frac{\delta Is}{Is_0}(x_\Omega)$$

where  $\theta$  is the diffraction angle derived from slowness vectors and  $\gamma_0$  is the ratio of  $S$ -velocity and  $P$ -velocity at  $x_\Omega$  in the reference medium. We can note that the contribution of the point  $x_\Omega$  is only taken into account if the dip perpendicular to the sum of the slowness vectors has been selected in the modelling parameters [17].

The perturbations  $[\delta Ip/Ip_0, \delta Is/Is_0, \delta\rho/\rho_0]$  are discretized on fine parallelepiped meshes  $[\delta x, \delta y, \delta z]$ . On the other hand, the Green quantities are calculated on coarse parallelepiped meshes  $[\Delta x, \Delta y, \Delta z]$  of the target. In order to obtain the contributions of the perturbations in the trace, the Green

quantities are interpolated for the fine meshes using the slowness vector derivatives. The reflection events are correctly built for a dip thin plate discretized in parallelepiped meshes if the mesh is fine enough. More precisely, the  $(x, y, z)$  dimensions of the mesh must respect some criteria which depend on the significant wavelength  $\lambda$  of the  $P$ -wave propagated field:  $\delta x$  and  $\delta y$  are required to be less than  $\lambda/8$ ,  $\delta z$  is required to be less than  $\lambda/16$ .

In addition, several works have proved that the Born modelling is not accurate for large incidence angles [18, 19, 8].

**2.1.2 Modelling Parameters**

The features of the 4D elastic model are that the reservoir zone is very heterogeneous and that the overburden zone is close to a stratified medium. Each of the four models is defined in  $P$ -velocity,  $S$ -velocity and density from the surface to the bottom of the reservoir (Fig. 5). The extensions of the model are  $Y = 1\,970$  to  $2\,790$  m and  $X = 712$  to  $812$  m in our local coordinate system. The models are initially discretized with a sampling of  $0.484$  m in depth,  $20$  m in the  $Y$ -direction

(parallel to the well paths), and  $1$  m in the  $X$ -direction (perpendicular to the well paths). The well paths are located around the depth of  $310$  m.

Acquisition parameters are selected to image a  $100$  m wide and  $820$  m long target, the target depth thickness remaining that of the reservoir model (close to  $50$  m). In doing so, the image will contain the entire well pair. We used an example of a dense land acquisition survey design, described in Figure 6. The source area located right above the target is included in the receiver area, which is larger. Sources and receivers are at the ground surface. The receivers record the vertical displacement of the computed wavefield. The source type considered is a vertical point force whose signature is a  $5$ - to  $320$ -Hertz band-pass. For each model, we handled a 3D seismic profile of  $336$  shots with  $1\,550$  fixed receivers.

In the ray+Born modelling technique, the reflection traveltimes, as well as the geometrical spreading, are governed by the reference model, whereas the reflection amplitudes are mainly linked to the perturbations of the target. Special attention is paid to the smoothing of the full

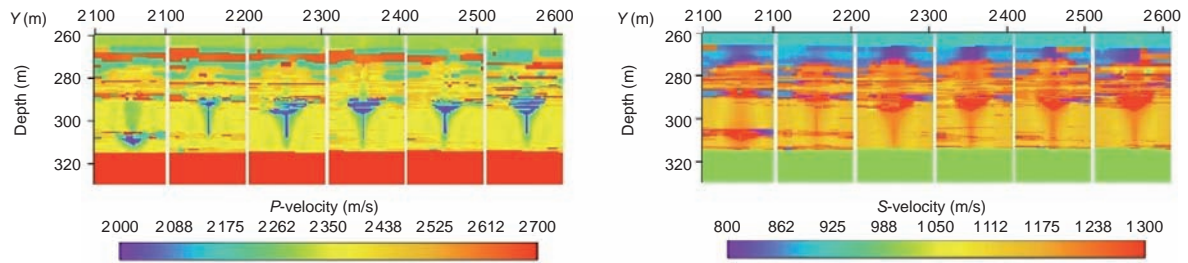


Figure 5

Velocity model ( $Y$ -sections perpendicular to the well paths) at 3rd year of production:  $P$ -velocity (left),  $S$ -velocity (right).

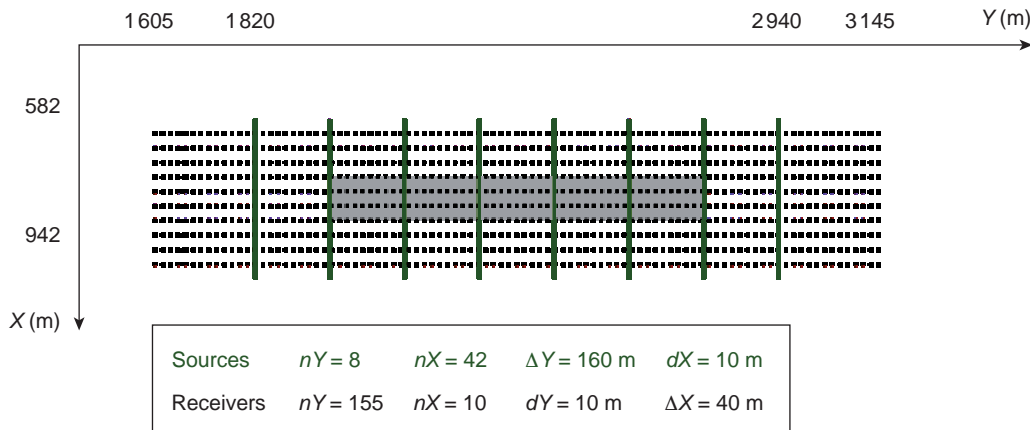


Figure 6

Surface acquisition pattern (sources in green, receivers in black) and target location (shadow zone,  $820$  m long by  $100$  m wide).

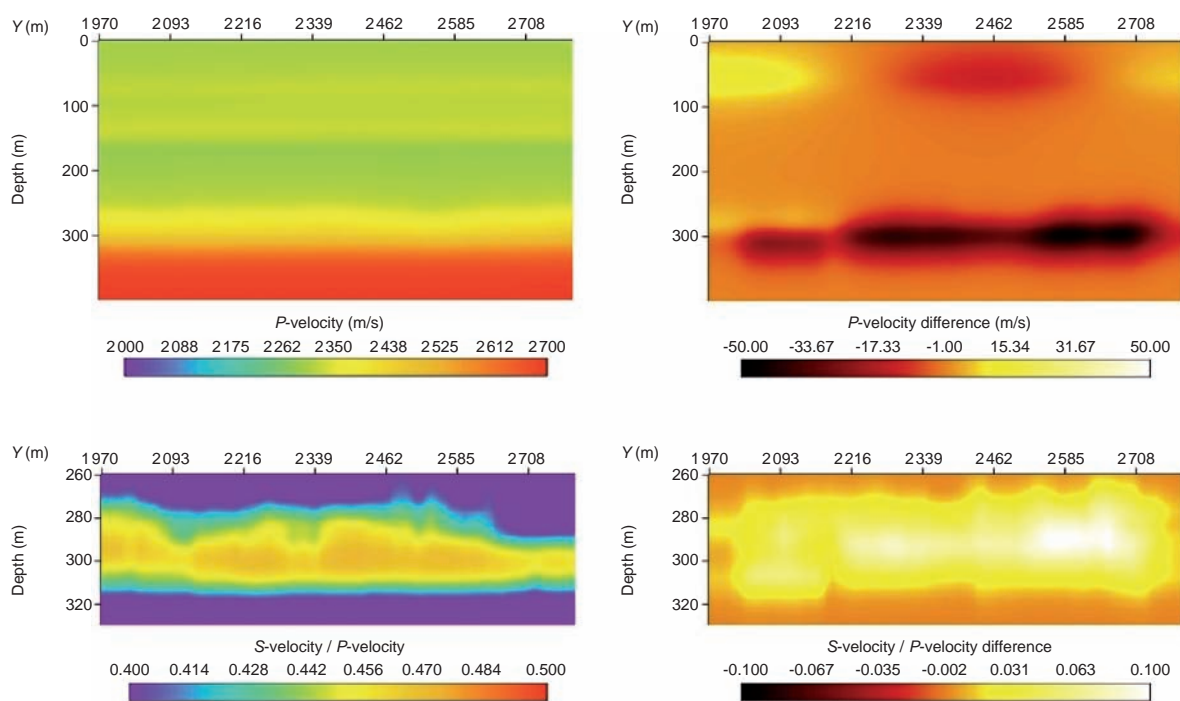


Figure 7

Smoothed models (section  $X = 762$  m parallel to the well paths) at initial stage (left), 3rd year of production minus initial stage (right):  $P$ -velocity (top), velocity ratio  $\gamma_0$  (bottom).

model because the surface-target traveltimes differences between successive stages of production must be preserved. The four 3D SAGD well pair velocity models going from the surface to below the reservoir are smoothed one by one. Dealing with  $P$ -wave reflections, the smooth reference model must only be defined in  $P$ -velocity for the full domain.

At this stage of the work, we controlled that the traveltimes differences between the four models remain after smoothing. We observed time differences in the range of 1 ms, which corresponds to the mean range that could be expected according to the  $P$ -velocity models converted in time.

Once the reference model is built, the  $P$ -impedance,  $S$ -impedance and density perturbations of the target are computed. For each model, the perturbations  $[\delta I_p/I_{p_0}, \delta I_s/I_{s_0}, \delta \rho/\rho_0]$  must be defined on a fine mesh in the target zone. The smoothed  $S$ -velocity and  $P$ -velocity ratio  $\gamma_0$  is also needed in the target zone.

As we were dealing with a maximum frequency of 320 Hz and a mean velocity of 2 500 m/s in the target, we needed to take a fine mesh of dimensions  $\delta x = \delta y < 0.97$  m and  $\delta z < 0.48$  m. We chose  $\delta x = \delta y = 1$  m and  $\delta z = 0.484$  m in order to have to resample only in the  $Y$  direction.

The smoothed density and the smoothed velocity ratio were derived from the smoothed impedances and  $P$ -velocity:  $\rho_0 = I_{p_0}/V_{p_0}$  and  $\gamma_0 = I_{s_0}/I_{p_0}$  (Fig. 7).

The relative perturbations were then computed and we obtained average values less than 0.1 for  $P$ -impedance and  $S$ -impedance and less than 0.04 for density. But for the third year of production model, we obtained some individual  $S$ -impedance perturbation values greater than 0.1 (Fig. 8) because of some strong  $S$ -velocity contrasts between sands and shales at this stage of production. That is why we performed an additional test of the Born modelling validity in this case. We calculated one shot using the ray+Born modelling for a 1D column and for a 2D section of the model corresponding to the high  $S$ -impedance relative perturbations. These  $P$ -wave shot gathers were compared to the full-wave shot gathers modelled with the help of finite-difference modelling (Fig. 9, 10). Though some high values of  $S$ -impedance perturbations are present, we concluded that the Born modelling is still valid for near and medium offsets in our case.

Different sizes of coarse meshes were tested:  $20 \times 20 \times 9.68$  m<sup>3</sup> and  $15 \times 15 \times 4.84$  m<sup>3</sup>. We selected the lower size because 1D target results obtained by ray+Born modelling fit well with the ones obtained by 3D full-wave modelling in a stratified medium.

Another point that we paid attention to is the dip of reflectors to be simulated. The target model at the 3rd year of production presents the strongest dip on the edge of the V-shaped steam chamber. The dip could rise there to 30 degrees. So we took

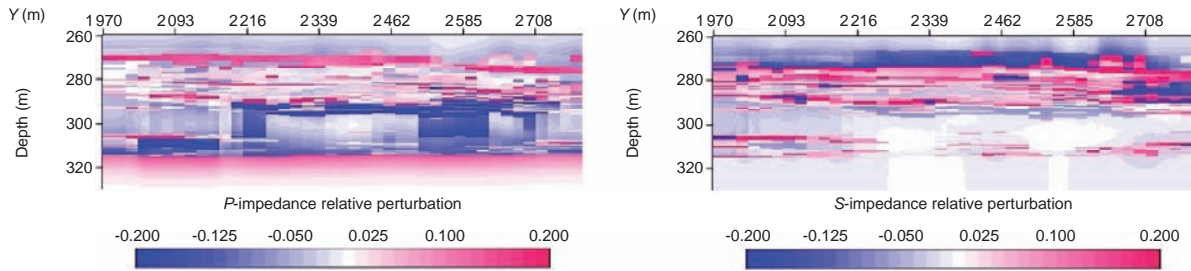


Figure 8

Perturbation models (section  $X = 762$  m parallel to the well paths) at 3rd year of production:  $P$ -impedance relative perturbation (left),  $S$ -impedance relative perturbation (right).

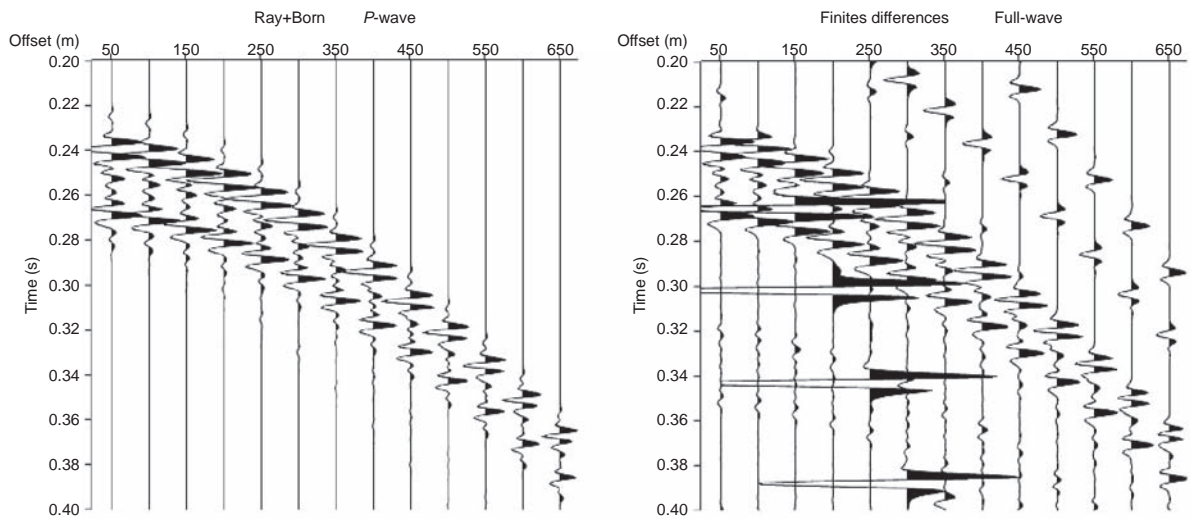


Figure 9

Model with high  $S$ -impedance perturbation values: ray+Born (left) versus Finite differences (right). 1D model (column  $X = 752$  m  $Y = 2780$  m, 3rd year of production). 130 Hz Ricker wavelet.

into account, during the modelling process, a dip aperture limited to 40 degrees.

## 2.2 Pre-Stack Seismic Data

### 2.2.1 Seismic Results

For each of the four production stages, shot gathers were then modelled according to the chosen acquisition geometry. The generated seismic traces are thus free of noise and contain only primary reflections originating from the reservoir zone (no surface, multiple or converted waves).

The synthetic data obtained with the 3D ray+Born modelling are multi-offset and multi-azimuth seismic datasets. Each 3D

shot gather contains 1550 seismic traces. Figure 11 shows part of a shot gather located at the acquisition center. As the Born modelling breaks down for large incidence angles, it is necessary to deal with a limited offset range (0 m to around 600 m).

The models of the four stages of production used for the seismic modelling exhibited differences in the reservoir zone. As observed for models, there were more significant differences in the seismic data between the 3rd year of production and the initial stage. We looked at the differences induced in the synthetic shot gathers in order to verify that the 4D effect is present in time-lapse and in amplitude variation. It can be noted that the maximum time difference is very small (close to 1 ms). On the other hand, seismic amplitude variation is stronger (Fig. 12).

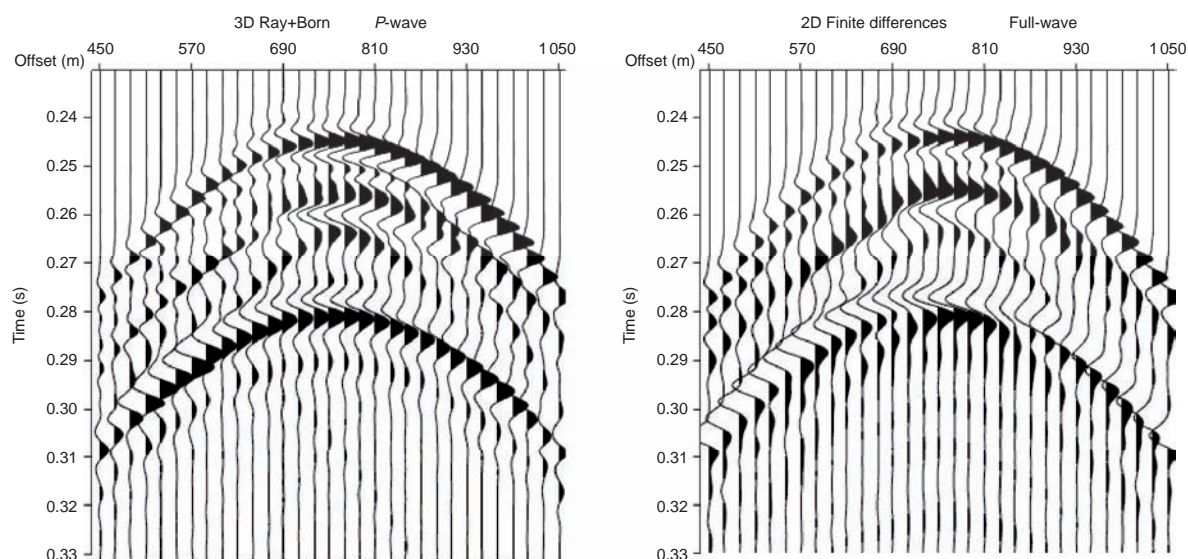


Figure 10

Model with high  $S$ -impedance perturbation values: ray+Born (left) versus Finite differences (right). 2D model (section  $Y = 2\,600$  m perpendicular to the well paths, 3rd year of production). 130 Hz Ricker wavelet (2D wavelet shape for Finite differences).

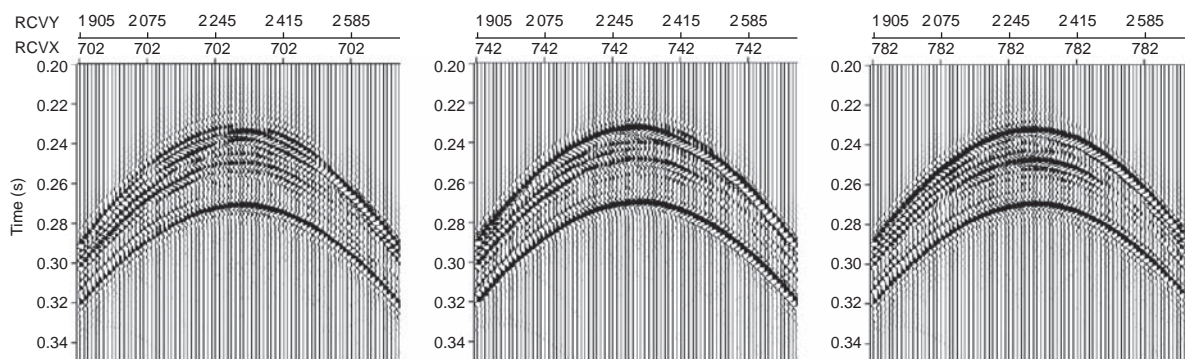


Figure 11

Synthetic shot gather at  $Y = 2\,300$  m,  $X = 767$  m at 3rd year of production: receivers at  $X = 702$  m,  $X = 742$  m and  $X = 782$  m (from left to right).

### 2.2.2 Adding Noise

Our aim was to add realistic noise on prestack seismic data. Two kinds of noise can be encountered for real data: random and coherent. The random noise is generally present with a signal to noise ratio lower for large offsets than for near offsets. The coherent noise often comes from a physical or mechanical event.

For the first work on these synthetic data, we chose to take into account only random noise. We used random noise data recorded by receivers during a real acquisition survey. Four different noise gathers were required for the synthetic prestack

data (one gather per stage of production). For each stage, we added random noise on synthetic prestack seismic data with a frequency-dependent signal-to-noise ratio: around 0 dB for frequency 50 Hz and 10 dB for frequencies 120-200 Hz (Fig. 13).

## 2.3 Seismic Processing

### 2.3.1 Process Workflow

The noise-free data are processed to get stacked and time migrated images in order to be able to run a seismic interpretation study in relation with the SAGD production as described

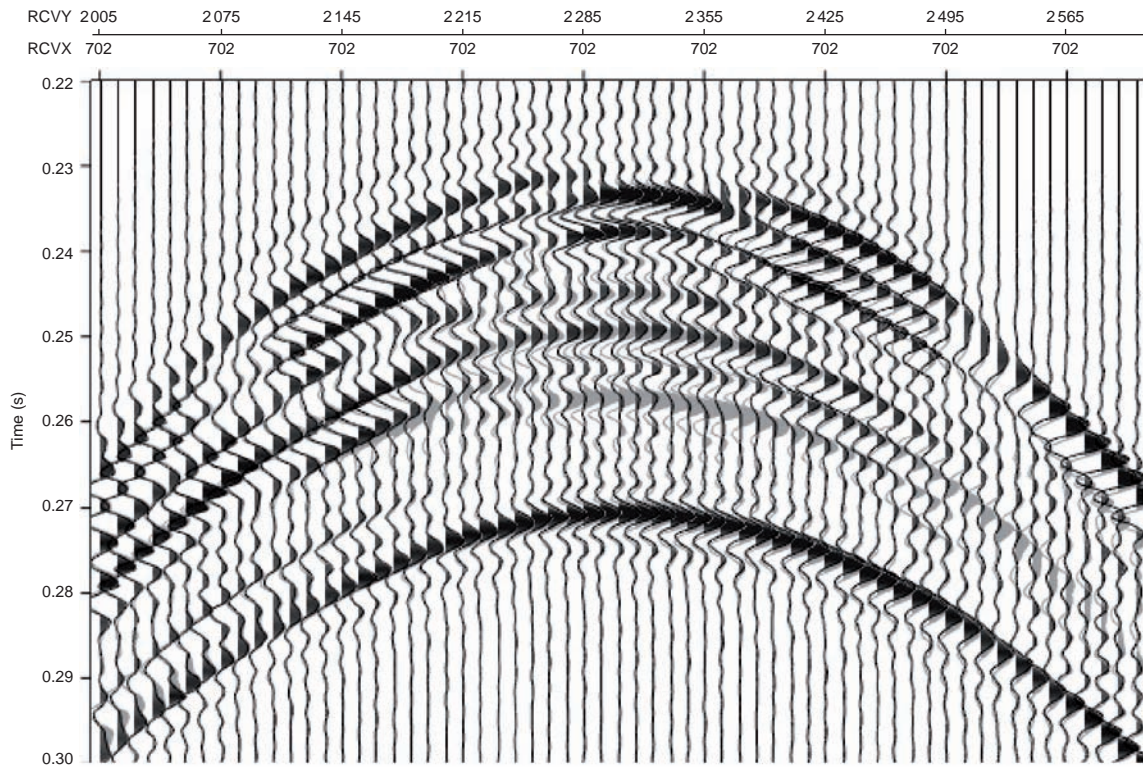


Figure 12

Shot gather located at  $Y = 2\,300$  m,  $X = 767$  m: initial stage (black color) and 3rd year of production (grey color).

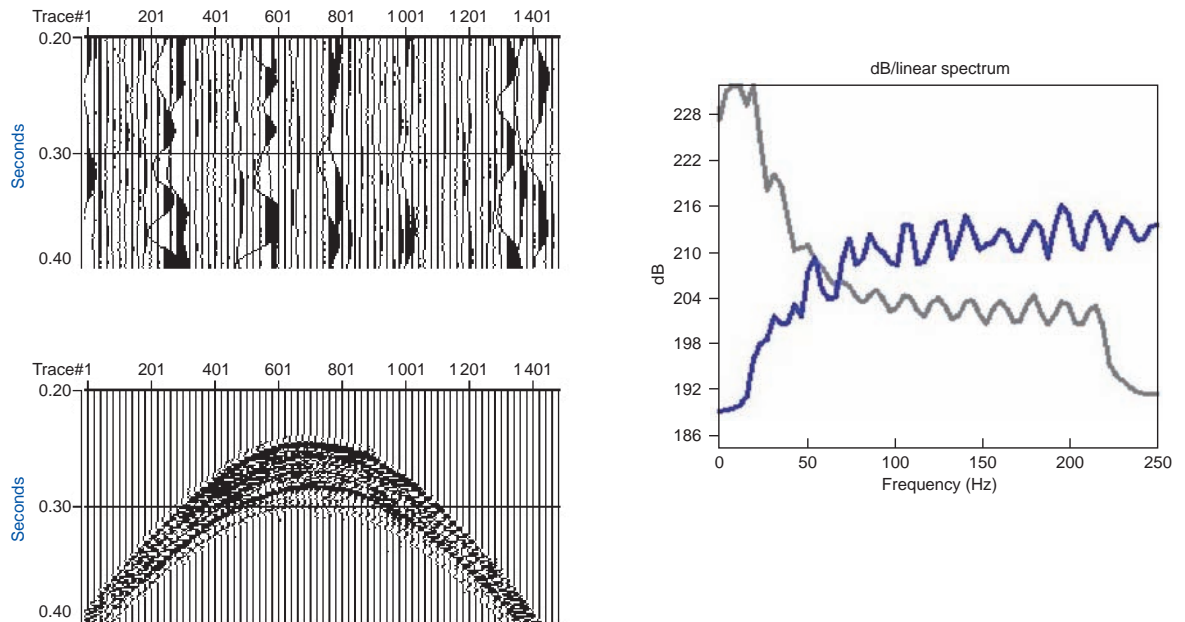


Figure 13

Comparison of amplitude spectrum of modelled shot (blue color) and noise data (grey color) at initial stage: difference of 0 dB at 50 Hz and of 10 dB at 200 Hz.

in the second part of this paper. We used a commercial software for the processing of the 4D seismic dataset. The synthetic data obtained with the 3D ray+Born modelling contain only the  $P$ -wave reflections that occur in the target reservoir zone. That is why we could perform a simple but robust processing workflow for each stage of production:

- first, we binned the traces with a bin size equal to  $5 \times 5$  square meters. The seismic dataset was then sorted by Common Mid Point (CMP) position defined by  $X$  and  $Y$  locations;
- secondly, we applied a normal moveout correction on each CMP with a RMS velocity model derived from the smoothed  $P$ -velocity model used in the modelling. The smoothed velocity differences of around  $-50$  m/s between the third year of production and the initial stage led to RMS velocity differences of around  $-10$  m/s. The corrected traces were stacked for the near offset range from 0 to 300 m;
- finally, we needed to perform a 2D time migration on the stacked sections, as many diffraction events are visible in the  $Y$  direction. This fact was strongly visible for the 3rd year of production where the dip of the steam chamber edges is thirty degrees. We applied the migration on all the  $Y$  sections of the stack that are perpendicular to the well paths.

In order to be able to study the effect of noise on interpretation results, the same processing workflow as for the noise-free data was performed on noisy data. But several “smiles” of migration were obtained due to the high energy of local noise events. That is why we needed to filter the low frequencies of the noisy synthetic data. In addition, it has been decided to filter the high frequencies in order to be closer to a real acquisition. A band-pass filter of 5-20-200-220 Hz has been applied to the noisy data before migration and also to the noise-free data in order to obtain comparable data.

### 2.3.2 Post-Stack Seismic Data

The processing workflow allowed us to obtain well focused reflectors for the noise-free data. The migrated stacks of the four stages are shown in Figure 14. There are no significant differences on the migrated stack between the initial stage and the first month of production for most of the CMP (Fig. 15). But at  $Y = 2100$  m, differences are visible just above the bottom of the reservoir around the location of the wells and could be related to the abnormal growth of the steam chamber (overpressured zone). Concerning the larger differences between the initial stage and the third year of production, they are more visible, on the lower right part ( $T \approx 0.265$  s) of the  $X = 760$  m section, around the heel of the wells, and on the upper middle part, above the well pair around the top of the steam chamber ( $T \approx 0.25$  s). As expected, the migrated stack of the noisy data was more biased than for the noise-free data. Particularly, some noise residuals appear like reflectors at the initial stage and the first

month of production stage (Fig. 16). The seismic interpretation presented in the second part of this paper will give more explanations of these differences. But, we must keep in mind that the large seismic coverage improves the resolution of both the seismic response and the seismic differences.

## 3 INTERPRETATION OF 4D SYNTHETIC SEISMIC DATA

Both noise-free and noisy synthetic migrated stacked seismic data were considered for interpretation, at the four available production stages. Let us remind that all seismic data are filtered with a band-pass of 5-20-200-220 Hz. In the following, we first briefly present the 4D synthetic seismic data as well as the reservoir/geomechanical properties issued from the model. Second, we present some of the interpretation results:

- computation of some seismic attributes from the synthetic seismic data;
- evaluation of the quantitative link (linear or not) of these attributes with the reservoir/geomechanical properties issued from the model;
- geobodies.

### 3.1 Available Reservoir/Geomechanical and Seismic Data

All figures in this part and Section 3.2 present inline section  $X = 760$  m of the seismic cube, from  $Y = 1970$  to  $2790$  m (820 m long) and from time 225 ms to 275 ms: this inline section is along the well pair path.

#### 3.1.1 Reservoir/Geomechanical Properties

Figure 17 shows (at initial stage and 3rd year of production) some of the reservoir/geomechanical properties that will be used for the interpretation of the seismic attributes: lithofacies, temperature, pore pressure, oil and steam saturations. Other reservoir/geomechanical properties like mean effective stress, volumetric strain and water saturation were also available for interpretation. All these properties are issued from the 4D geological model in depth: they were transferred in time according to the associated velocity model, and then rescaled on the seismic grid.

#### 3.1.2 Seismic Data

Figures 18 and 19 show the seismic amplitudes at the four production stages, respectively for noise-free data and noisy data. And Figure 20 present the seismic amplitude changes after one month and three years of production, computed on noise-free and noisy seismic data.

As can be seen from Figure 18 and Figure 20, there are already some amplitude changes after one month of production at the heel of the well pair: these changes are linked with the presence of a shale level just above the injector well

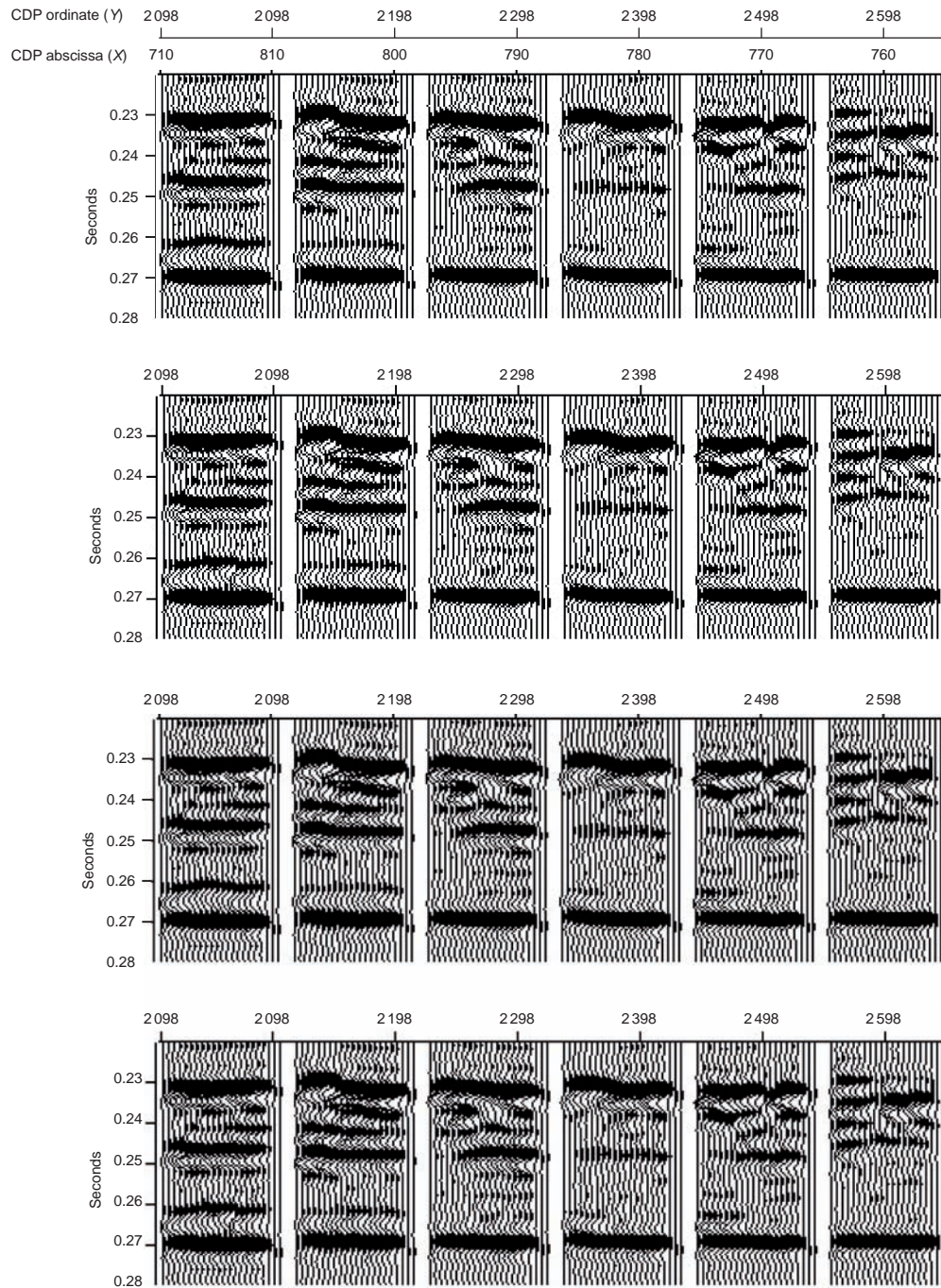


Figure 14

Noise-free migrated stack Y-sections: initial stage, 1st month, 6th month and 3rd year of production (from top to bottom).

(see Fig. 17a, b and Fig. 2). This shale level acts as a barrier and prevents the steam chamber to develop vertically; therefore, very early in the production, high pressure values appear above this level, due to the fact that fluids in the corresponding materials are heated by conduction but cannot

be produced; as well below the shale level, high mean effective stress values and high temperature values are observed. This impacts both densities and velocities, thus seismic amplitudes. These seismic amplitudes and delays changes at the heel of the well pair increase with calendar time.

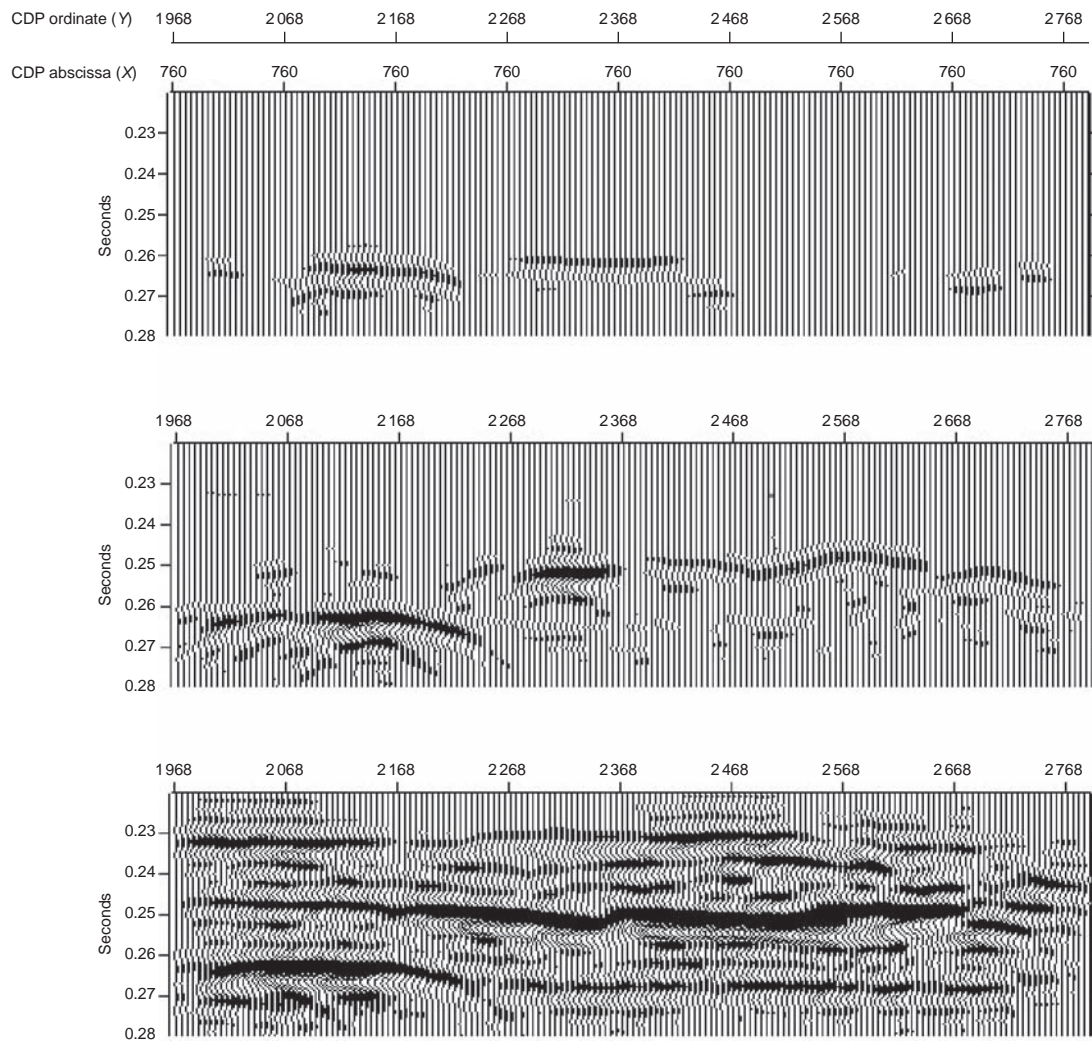


Figure 15

Differences of noise-free migrated stack X-section ( $X = 760$  m): 1st month of production (top), 6th month of production (middle), 3rd year of production (bottom) minus initial stage.

In the middle of the well pair, the reservoir is of very good quality, showing no shale levels above the well injector. In these areas, changes in the seismic character (amplitudes and delays) are mainly visible after the 6th month of production.

From Figures 19 and 20, it appears that the impact of the noise is very strong at all stages: for example the noise completely overrides the seismic changes at the beginning of production. Of course, on real seismic data, one would apply noise removal techniques before interpretation of the seismic data. However, the geometry and volume of the steam zone cannot be clearly delineated even on noise-free seismic data. Therefore, this call for the use of seismic derived attributes instead of the sole seismic amplitudes, when trying to interpret the seismic surveys in terms of geomechanical and reservoir properties along production.

### 3.2 Computation of Seismic Attributes

Several seismic attributes [20] were computed, *e.g.*:

- 3D attributes (energy, frequency filters, RMS values of amplitude changes between stages, attribute changes between stages, similarity);
- 2D attributes (maps of time differences between stages, reservoir traveltimes changes between stages).

Some of them are briefly discussed in the following in terms of production content, robustness to noise etc.

#### 3.2.1 Energy

This attribute enhances, among others, lateral variations within seismic events. The response energy also characterizes acoustic rock properties and bed thickness.

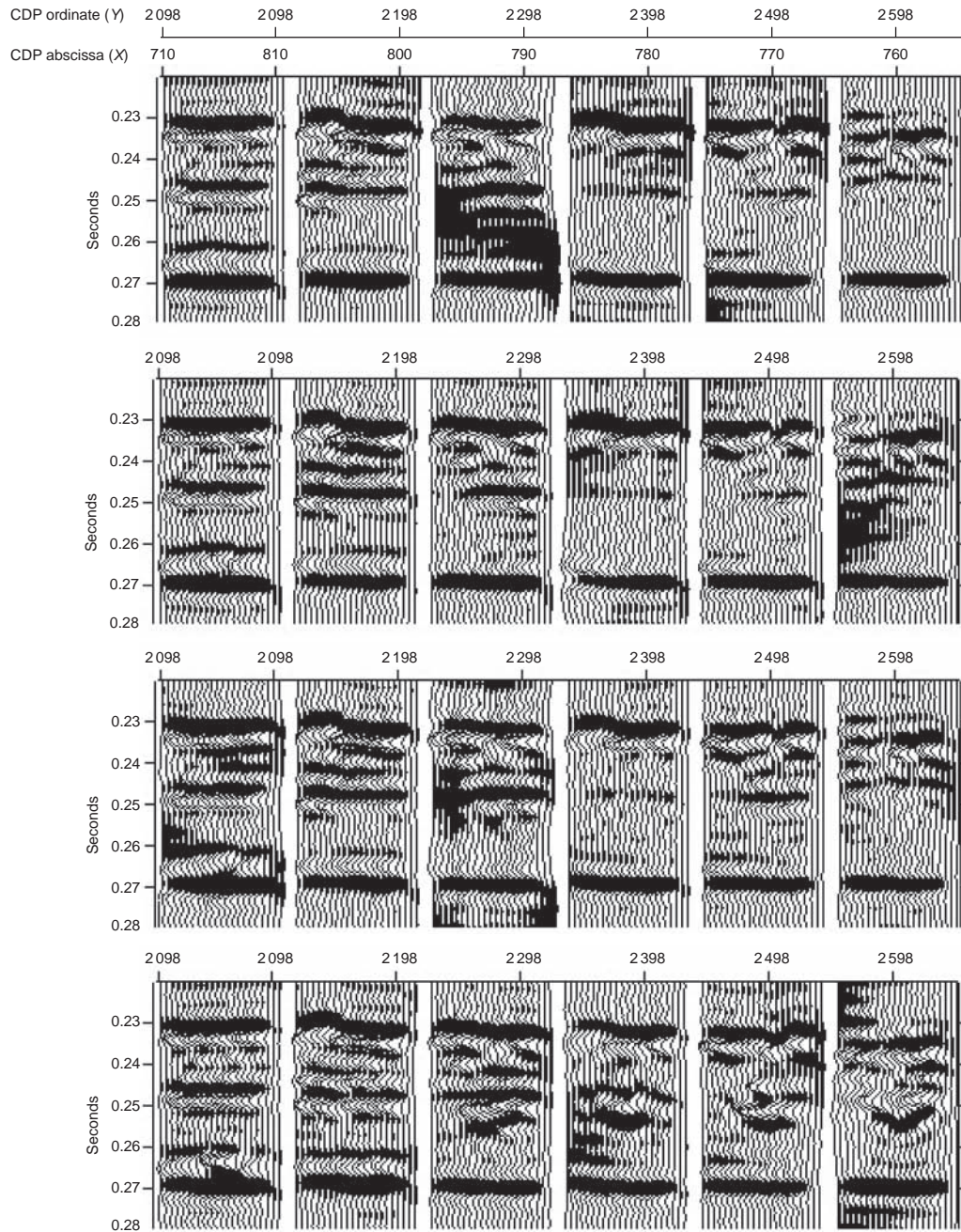


Figure 16

Noisy migrated stack Y-sections: initial stage, 1st month, 6th month and 3rd year of production (from top to bottom).

Figure 21 shows the energy on the noise-free and on the noisy data at initial stage and at 3rd year of production. First, we see that this attribute is sensitive to the production (change of energy between initial stage and third year of production) and robust to the noise: even if the noise is visible, it is not strong enough to override the change linked with production. Second, by comparing this figure to Figure 17

(lithofacies and for example steam saturation), we see that energy combines both reservoir information on lithology (high values of energy corresponding to shaly content at initial stage) and production effects.

To get rid of the lithology effect on energy, the changes of energy between the three production stages and the initial stage (see Fig. 22) were computed. The high values

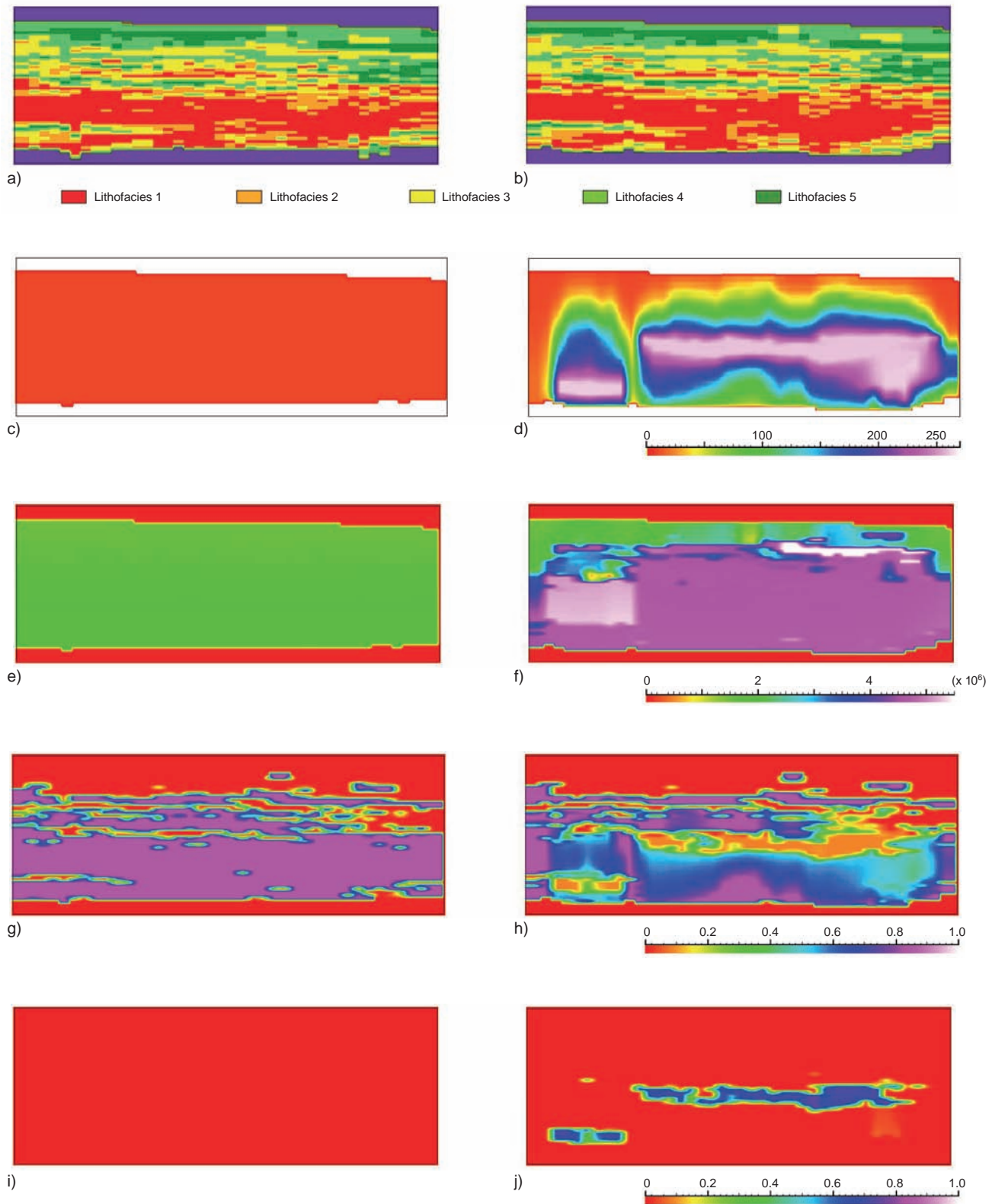


Figure 17

a) Lithofacies at initial stage; b) Lithofacies at 3rd year of production (see Lithofacies description in *Tab. 1*); c) Temperature in °C at initial stage; d) Temperature in °C at 3rd year of production; e) Pressure in Pa at initial stage; f) Pressure in Pa at 3rd year of production; g) Oil saturation at initial stage; h) Oil saturation at 3rd year of production; i) Steam saturation at initial stage; j) Steam saturation at 3rd year of production. Inline  $X = 760$  m along well paths of length 820 m, between 225 ms and 275 ms.

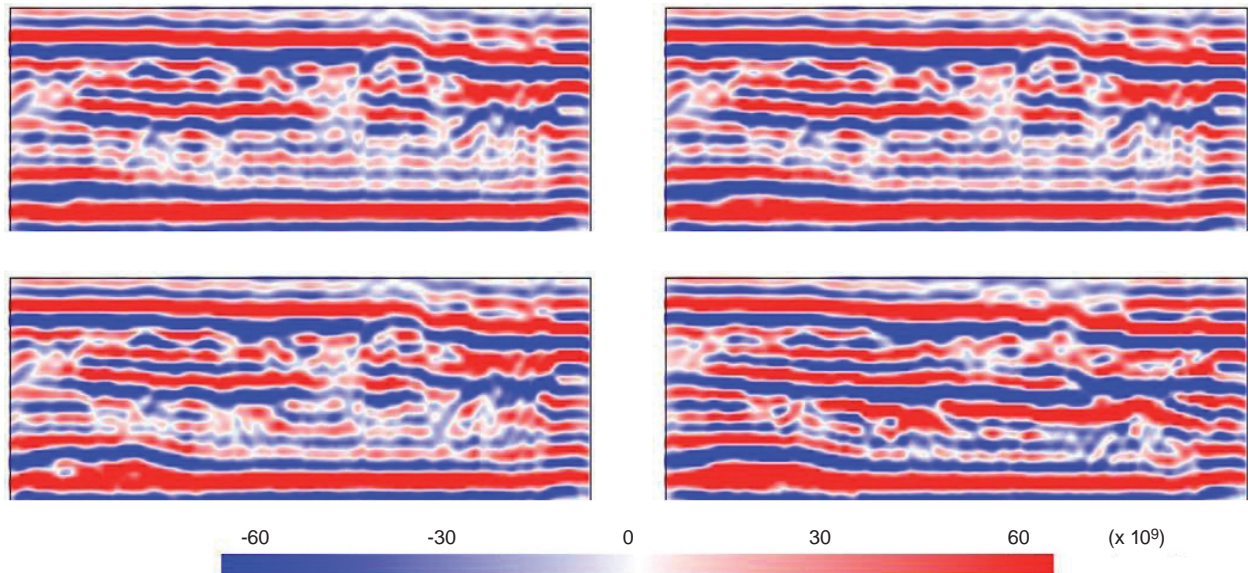


Figure 18

Noise-free seismic amplitudes after 5-20-200-220 Hz band-pass filter: initial stage (top left), 1st month (top right), 6th month (bottom left) and 3rd year of production (bottom right). Inline  $X = 760$  m along well paths of length 820 m, between 225 ms and 275 ms.

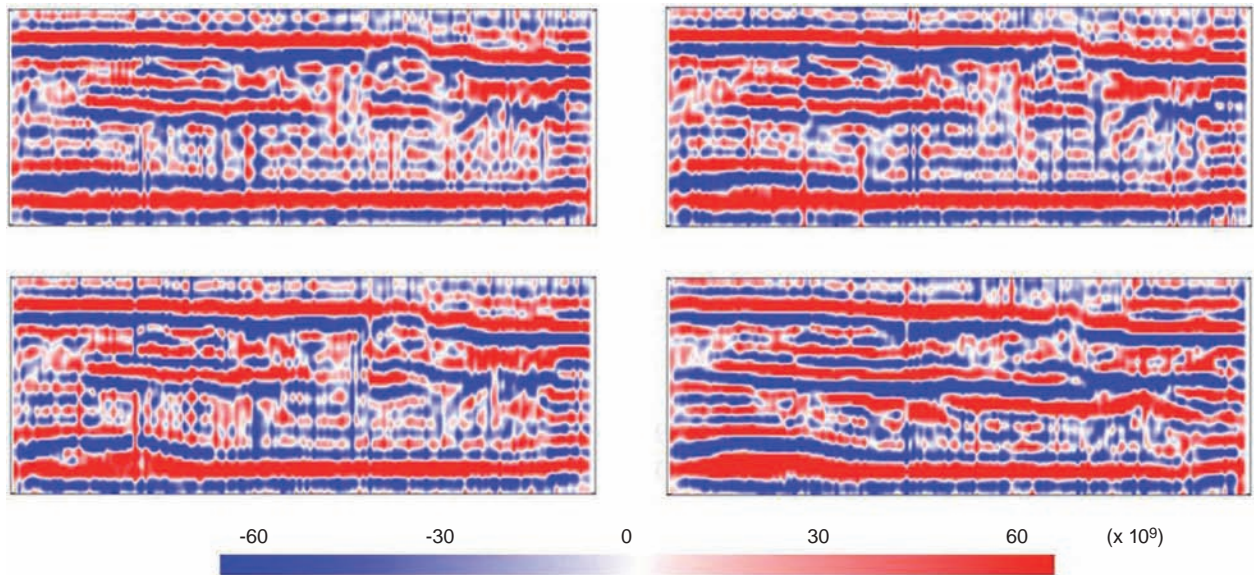


Figure 19

Noisy seismic amplitudes after 5-20-200-220 Hz band-pass filter: initial stage (top left), 1st month (top right), 6th month (bottom left) and 3rd year of production (bottom right). Inline  $X = 760$  m along well paths of length 820 m, between 225 ms and 275 ms.

of energy changes after three years of production can be visually linked to the steam saturation envelope (Fig. 17i, j). Thus, a cutoff on energy change could give an idea of the steam area.

According to the way the noise was added to the seismic data (*i.e.* independently from one stage to another), the energy change appears slightly sensitive to the noise.

### 3.2.2 Frequency Filters

Nine band-pass filters were applied on the noise-free and on the noisy data at the four production stages. To sample the whole seismic frequency range (10 Hz to 220 Hz) and preserve the same octave number, these band-pass filters were chosen as triangular as possible with frequency peaks at 10, 14, 20, 28, 40, 57, 81, 115, 163 Hz.

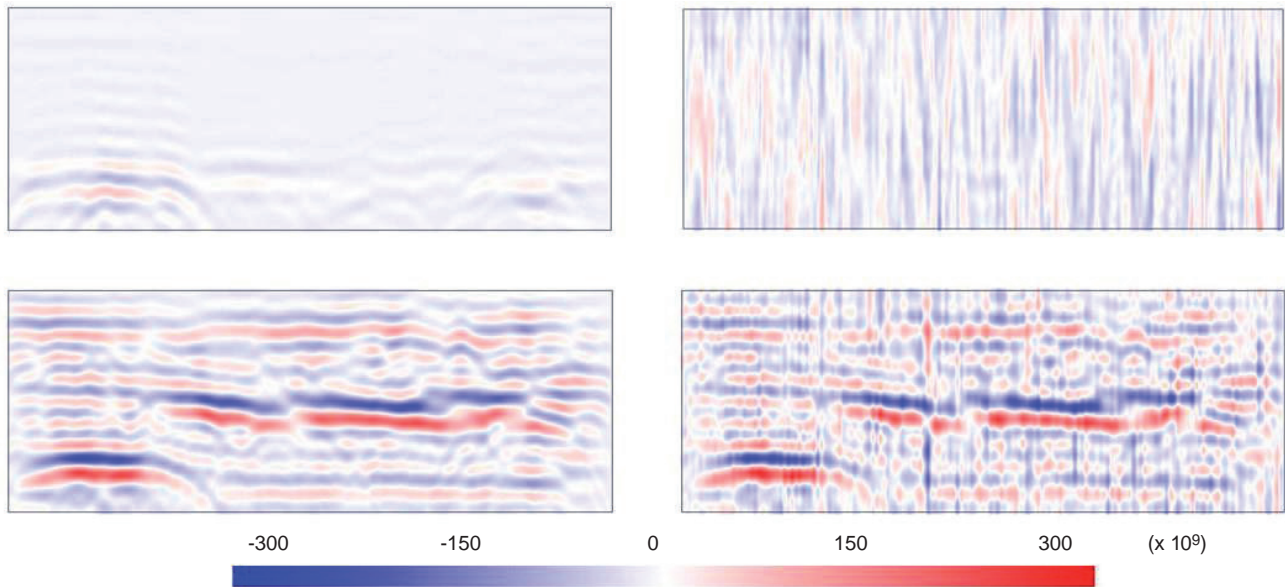


Figure 20

Seismic amplitude changes after one month of production (top), 3 years of production (bottom), computed on noise-free seismic data (left) and noisy data (right). Inline  $X = 760$  m along well paths of length 820 m, between 225 ms and 275 ms.

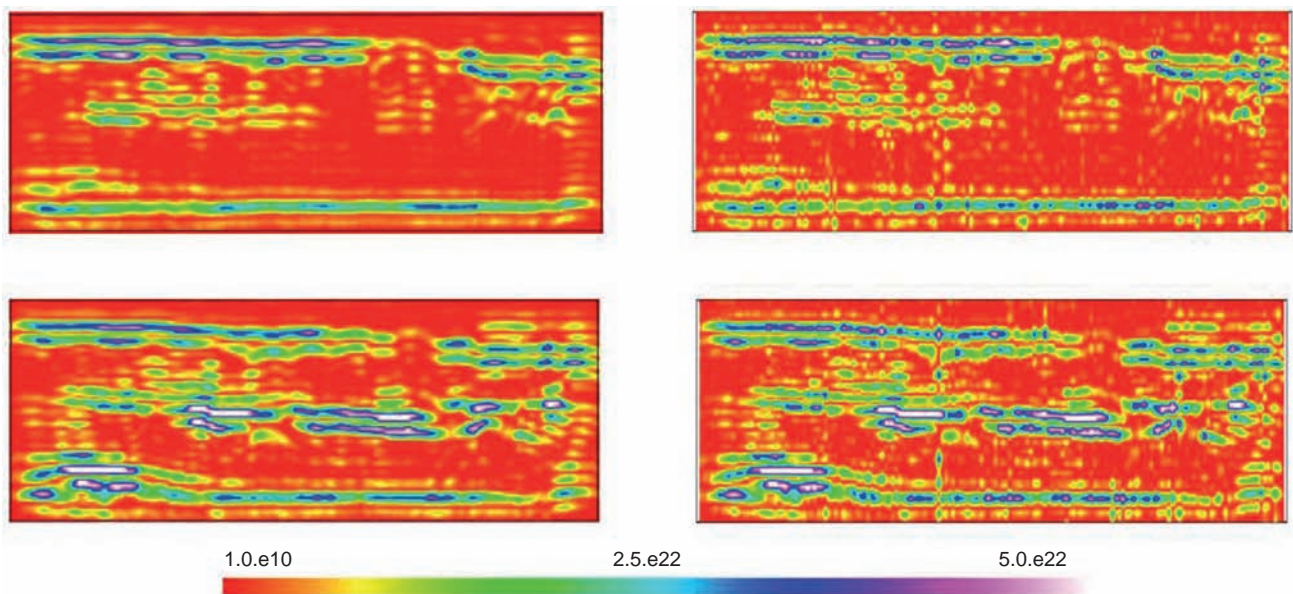


Figure 21

Energy at initial stage (top) and 3rd year of production (bottom), computed on noise-free seismic data (left) and noisy data (right). Inline  $X = 760$  m along well paths of length 820 m, between 225 ms and 275 ms.

Figure 23 shows the result for band-pass filters 28, 57 and 115 Hz on the noise-free data, respectively at initial stage and 3rd year of production. Results on noisy data are not given here. But from all results, one could see that:

- there is very little information up to the 20 Hz peak;
- the frequency filtered data are difficult to visually link with reservoir or production information;
- there is no visible production effect below the 28 Hz peak;
- above the 28 Hz peak, the production effect is increasing with frequency;

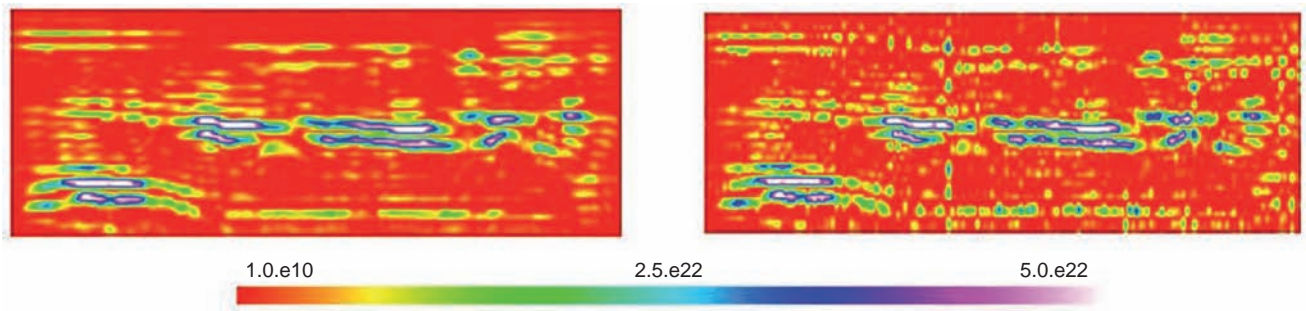


Figure 22

Changes of energy between 3rd year of production and initial stage, computed on noise-free seismic data (left) and noisy data (right). Inline  $X = 760$  m along well paths of length 820 m, between 225 ms and 275 ms.

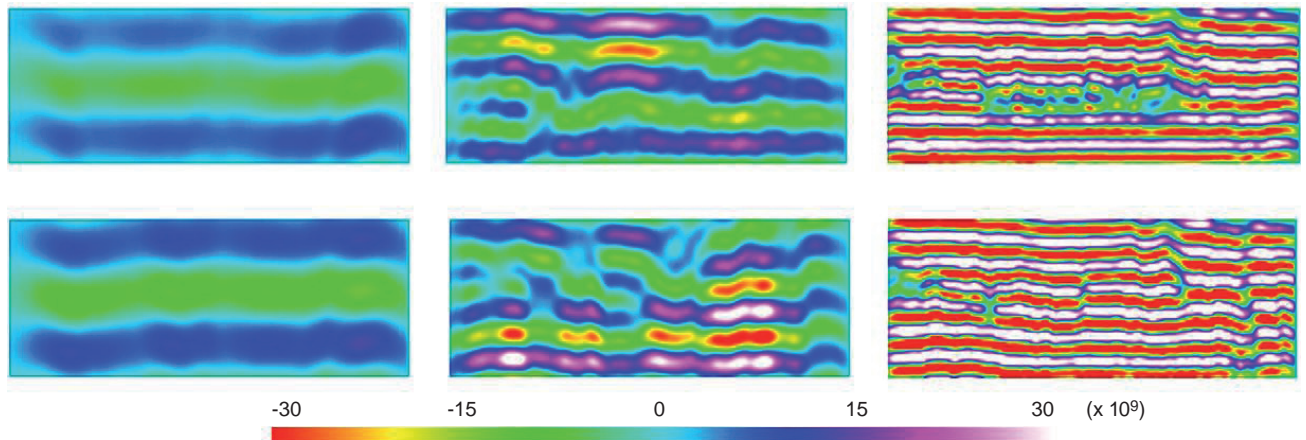


Figure 23

Frequency filtered data computed on noise-free seismic data: frequency peaks at 28 Hz, 57 Hz and 115 Hz (from left to right), at initial stage (top) and 3rd year of production (bottom). Inline  $X = 760$  m along well paths of length 820 m, between 225 ms and 275 ms.

- the noise strongly affects the seismic filtered data up to 20 Hz peak frequency and is clearly visible up to 57 Hz peak frequency (81 Hz maximum frequency), which is coherent with the noise frequency content;
- the noise overrides partly the production effect for low frequencies.

So, from these 4D synthetic seismic data, the frequency filter seismic attribute appears sensitive to the production effect but visually unlinked with reservoir/production properties. It is also sensitive to the noise, mostly at low frequencies. And the noise may override the production effect on the seismic, thus biasing further interpretations.

### 3.2.3 RMS Values of Amplitude Changes Between Two Production Stages

Root Mean Squared (RMS) values were computed on seismic trace amplitude changes between production stages and initial stage, over a local neighbourhood.

Figure 24 presents the RMS values of amplitude changes after one month of production and three years of production, on noise-free and noisy data.

We see that this attribute accounts for production. The higher values after one month of production (in green) correspond to the shale level at the heel of the well pair (see Fig. 17a, b) which prevents the steam to expand vertically. After three years of production, the higher values (in blue and purple) can be visually related to the highly steam saturated zone (Fig. 17i, j).

But unfortunately, this attribute appears very sensitive to the noise: this is critical at the beginning of production since the tiny production effects of the first month of production are completely overridden by the noise.

### 3.2.4 Computation of Time Differences Between Stages

In order to carefully estimate the time differences between any stage of production and the initial stage, the migrated stack

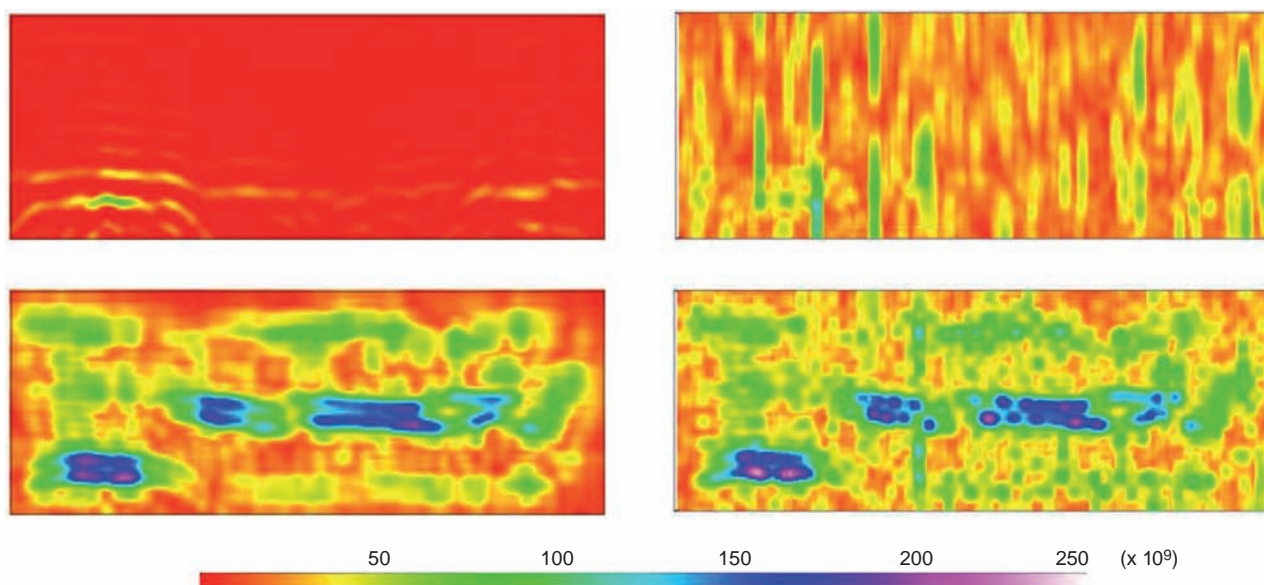


Figure 24

RMS values of amplitude changes between: 1st month of production and initial stage (top), 3rd year of production and initial stage (bottom), computed on noise-free seismic data (left) and noisy data (right). Inline  $X = 760$  m along well paths of length 820 m, between 225 ms and 275 ms.

cross-correlations of the three stages of production with the initial stage were first computed. This was performed for a time window of 20 ms around the reservoir top and around the reservoir bottom; the time of maximum auto-correlation of the initial stage was then subtracted to the three times of maximum cross-correlation.

Figures 25 and 26 show the corresponding time difference maps, respectively at top and bottom of the reservoir, between initial stage and three production stages, both for noise-free and noisy data.

These time differences between stages computed from the seismic data appear interesting to monitor the production, as well as are the reservoir traveltimes changes not shown here. The general trend is that time differences are negative at the heel of the well pair (where a shale level prevents the steam chamber to expand vertically toward the surface), and positive in the middle of the well pair.

At reservoir top (Fig. 25), the production effect is only visible after six months of production with time differences less than 0.13 ms in absolute values. At reservoir bottom (Fig. 26), local differences are already visible along the well paths for the first month of production (comprised between  $-0.6$  and  $0.28$  ms), and more accentuated for the sixth month of production (between  $-1.9$  and  $0.33$  ms). After the 3rd year of production, time differences reach  $-2$  ms at the heel of the well pair and 1 ms in the good reservoir area.

Noise has a very strong impact, mostly at the beginning of production and on the seismic cube borders (due to

insufficient stack fold). Therefore, using these attributes on real seismic data calls for a careful removal of the seismic noise. This is even more crucial at the early stages of production with very tiny production effects. However, the reservoir bottom time difference map can obviously help to delineate, very early in the production, the areas where the steam chamber cannot grow properly like the shaly area at the heel of the well pair (with strong negative time differences).

### 3.2.5 Seismic Attributes Summary

This brief description of a few seismic attributes already shows that some seismic attributes are visually/qualitatively related to the lithofacies, but more importantly to the geomechanical/production properties. Working on real seismic data, one would better use 3D attributes like energy or energy changes between stages, or 2D attributes like maps of time differences between stages at reservoir top/bottom, since these seismic attributes are more robust to seismic noise. Other seismic attributes like 3D cubes of time differences between stages, amplitude envelop, instantaneous frequencies/phases or spectral components should be evaluated for comparison.

### 3.3 Quantitative Relationships Between Seismic Attributes and Reservoir/Geomechanical Properties

The next step was to check out for potential quantitative links between the geomechanical/production properties and the

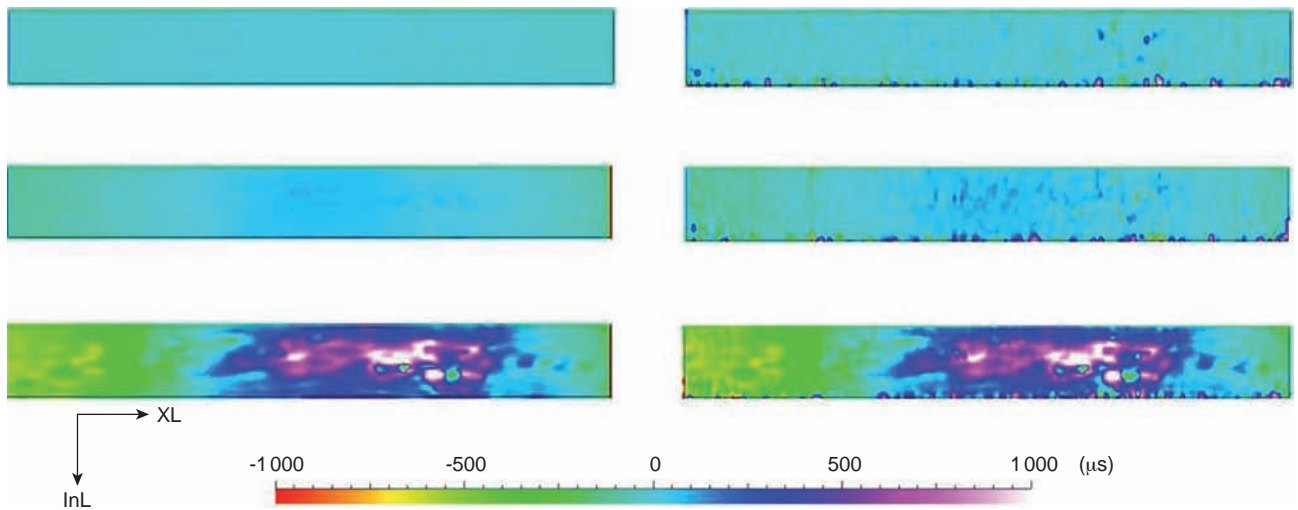


Figure 25

Map view of time differences at reservoir top (in microseconds) computed on noise-free seismic data (left) and noisy data (right): between 1st month of production and initial stage, 6th month of production and initial stage, 3rd year of production and initial stage (from top to bottom). Map of 100 m in InL and 820 m in XL.

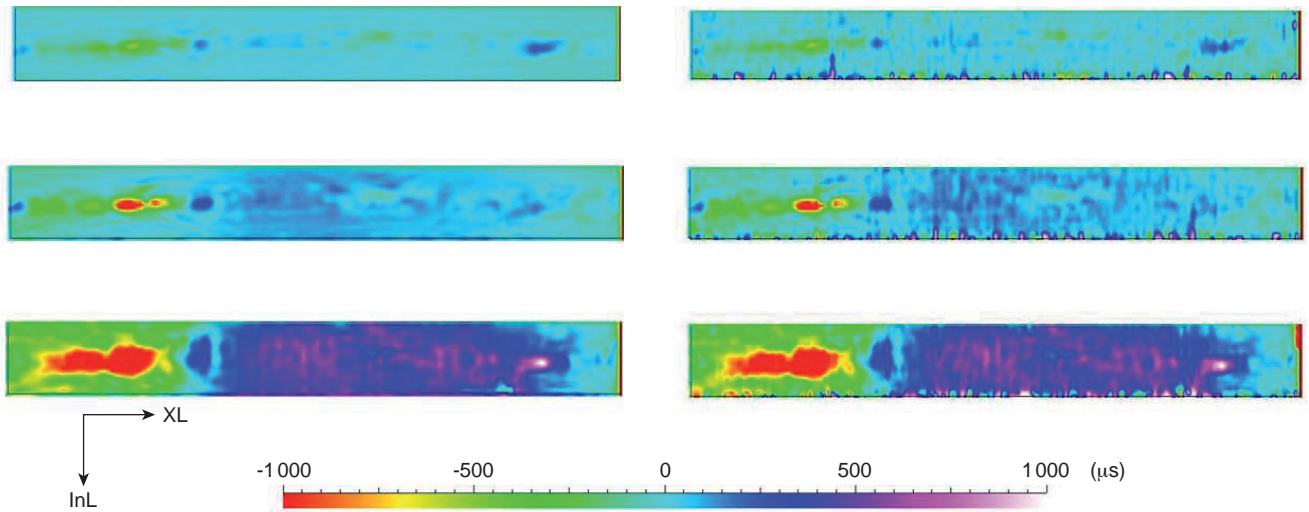


Figure 26

Map view of time differences at reservoir bottom (in microseconds) computed on noise-free seismic data (left) and noisy data (right): between 1st month of production and initial stage, 6th month of production and initial stage, 3rd year of production and initial stage (from top to bottom). Map of 100 m in InL and 820 m in XL.

seismic attributes (or seismic attribute changes between stages). The best linear correlation amongst any pair of seismic attribute and geomechanical/production property is of 0.66, between temperature and RMS values of amplitude changes (based on noise-free seismic data). The other correlations do not exceed 0.35 which means no linear correlation at all. To check out for potential non linear relationships, the

seismic attributes were crossplotted *versus* any of the geomechanical/production property. For example, Figure 27 shows these crossplots for steam saturation and temperature. For steam saturation, the noise-free seismic attributes are the amplitudes (named *Ampl*), the frequency filters at peaks 28, 57 and 115 Hz (named *f28*, *f57*, *f115*) and the energy (named *Energy*). For temperature, we consider the changes between

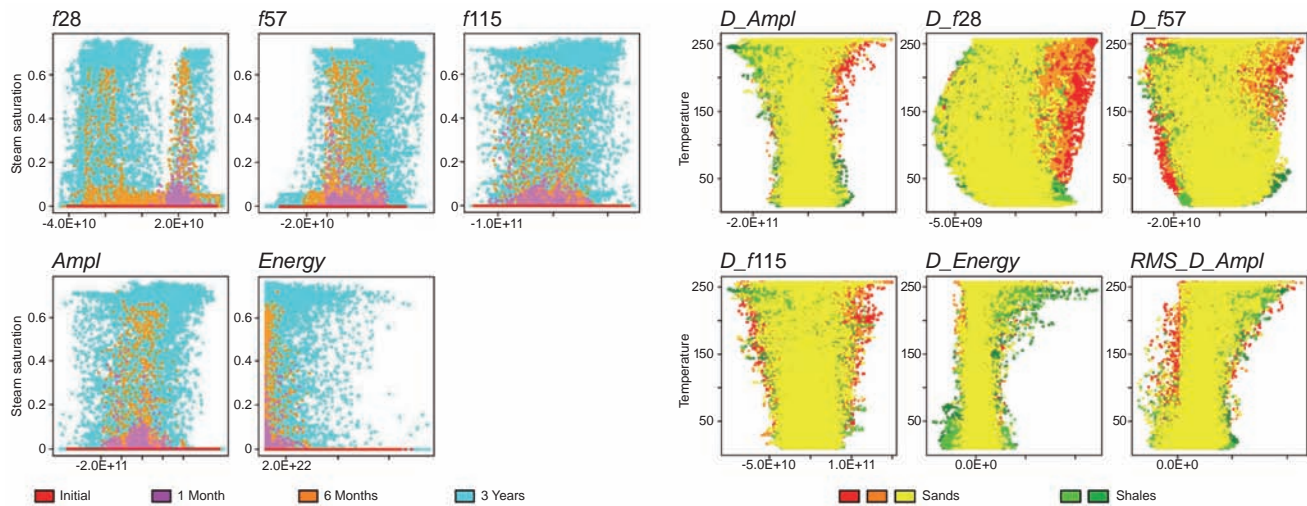


Figure 27

Crossplots of noise-free seismic attributes *versus* steam saturation colour-coded according to stage (left), and of noise-free seismic attributes changes *versus* temperature colour-coded according to lithofacies (right).

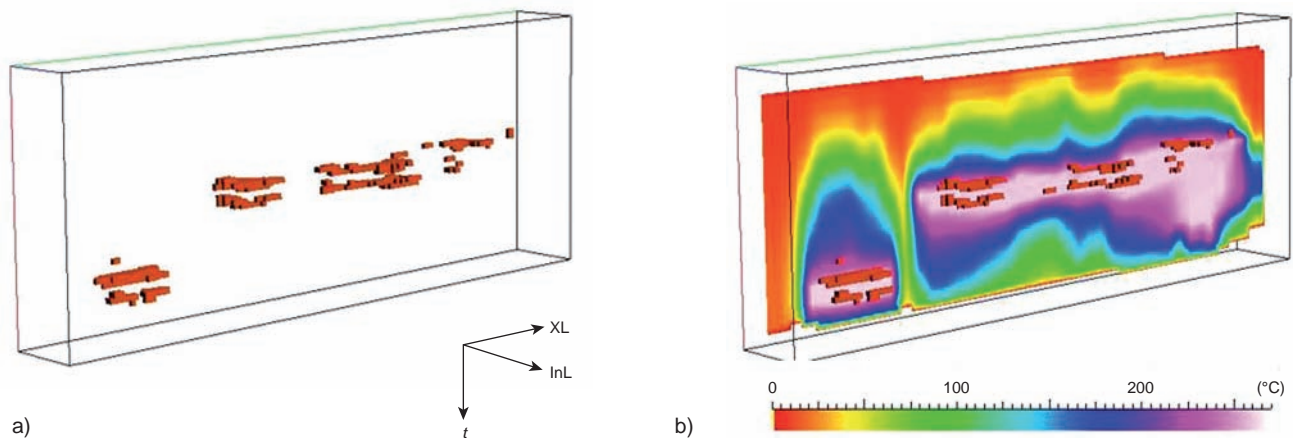


Figure 28

Geobody based on noise-free seismic energy changes, after 3 years of production. a) 3D view; b) Geobody over temperature (in °C) at inline  $X = 760$  m. Cube of 100 m in InL, 820 m in XL, from 225 ms to 275 ms.

stages from noise-free data: the amplitude changes (named  $D\_Ampl$ ), the three frequency filters changes (named  $D\_f28$ ,  $D\_f57$ ,  $D\_f115$ ), the energy changes (named  $D\_Energy$ ) and the RMS values of amplitude changes (named  $RMS\_D\_Ampl$ ). As can be seen, the relationships are of poor quality and cannot be used for estimating the geomechanical/production properties from the seismic attributes: the conclusion is the same for all others crossplots, things being even worst when considering noisy seismic data. Accounting for the lithofacies or the production stage does not improve the relationships. Thus, even if some seismic attributes appeared to be visually/qualitatively linked with the geomechanical/

production properties, they are not quantitatively related to them. This confirms the need for PetroElastic or Rock Physics Modelling when trying to quantitatively interpret 4D seismic data of heavy oil reservoirs produced with SAGD.

### 3.4 Geobodies

Two geobodies based on cutoffs (defined from the crossplots) on specific seismic attributes are proposed here.

The first geobody is based on a cutoff on the energy changes between stages, keeping only values higher than  $4.2e22$ . Figure 28 shows the corresponding geobody from

noise-free seismic data for three years of production. As shown, this geobody corresponds to high values of temperature (greater than 157°C) and provides partly the top of the steam chamber. But it is slightly sensitive to noise (Fig. 29); and it is not efficient at the early stages of production, since no geobody can be extracted up to 6 months of production.

A second geobody has been established from a principal component analysis. A principal component [21] is a specific linear combination of attributes. In our case, the first principal component *Prin1* is based on the seismic attributes changes

between stages (mainly on seismic amplitudes and higher frequency filters at peaks 57 and 115 Hz) and can be expressed as:

$$Prin1 = 0.69 \times D\_Ampl_{St} + 0.61 \times D\_f115_{St} + 0.32 \times D\_f57_{St} + 0.18 \times RMS\_D\_Ampl_{St} + 0.12 \times D\_f28_{St} + 0.09 \times D\_Energy_{St}$$

where  $D\_Ampl_{St}$ ,  $D\_f115_{St}$ ,  $D\_f57_{St}$ ,  $RMS\_D\_Ampl_{St}$ ,  $D\_f28_{St}$  and  $D\_Energy_{St}$  correspond respectively to the following standardized seismic attributes: amplitude changes between

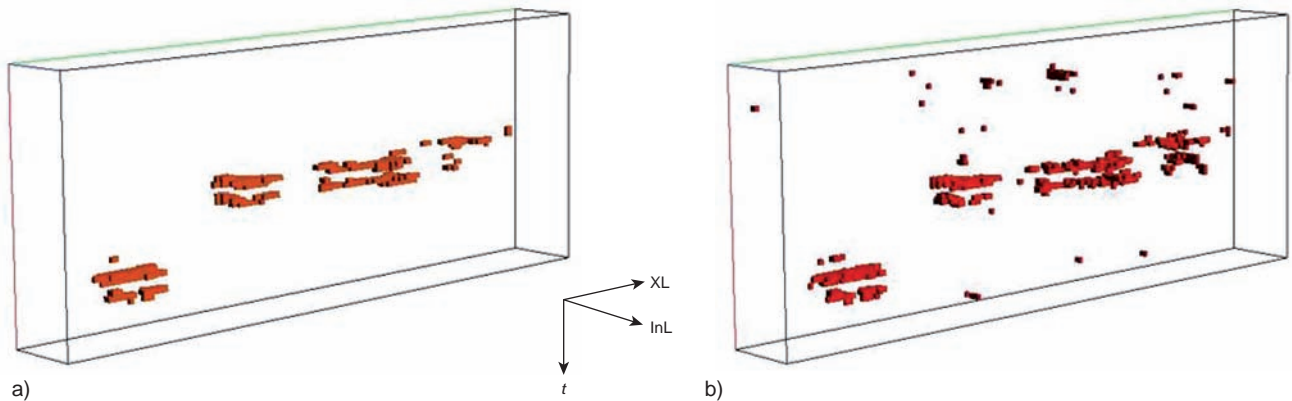


Figure 29

Geobody based on energy change after 3 years of production computed on a) Noise-free seismic data, b) Noisy seismic data. Cube of 100 m in InL, 820 m in XL, from 225 ms to 275 ms.

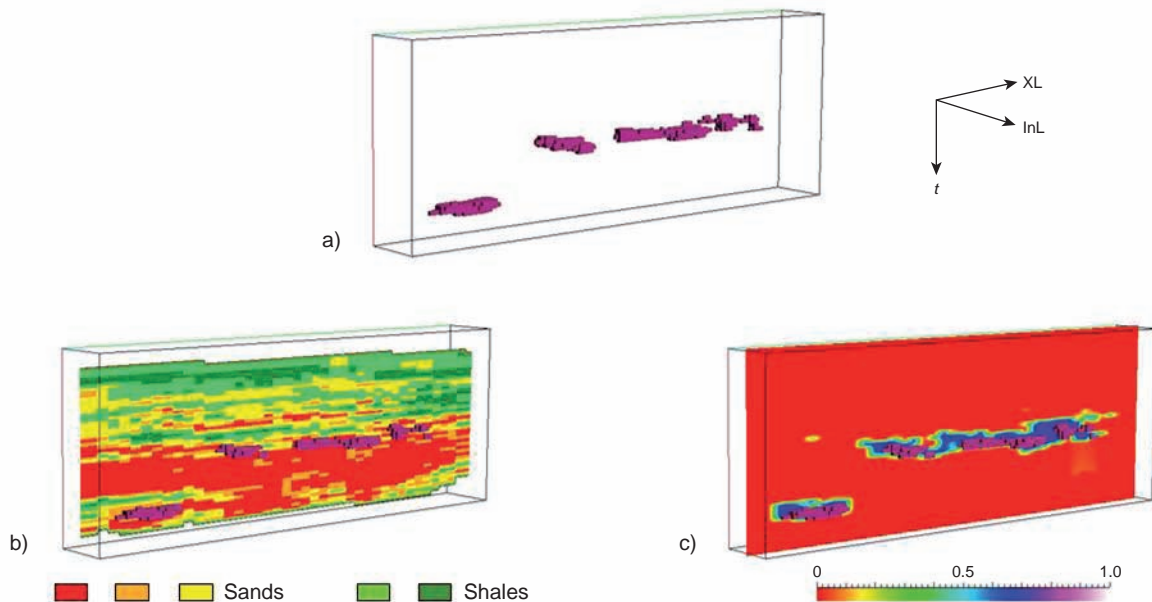


Figure 30

Geobody based on first principal component from noise-free seismic attribute changes between stages, after 3 years of production. a) 3D view; b) Geobody over lithofacies at inline X = 760 m; c) Geobody over steam saturation at inline X = 760 m. Cube of 100 m in InL, 820 m in XL, from 225 ms to 275 ms.

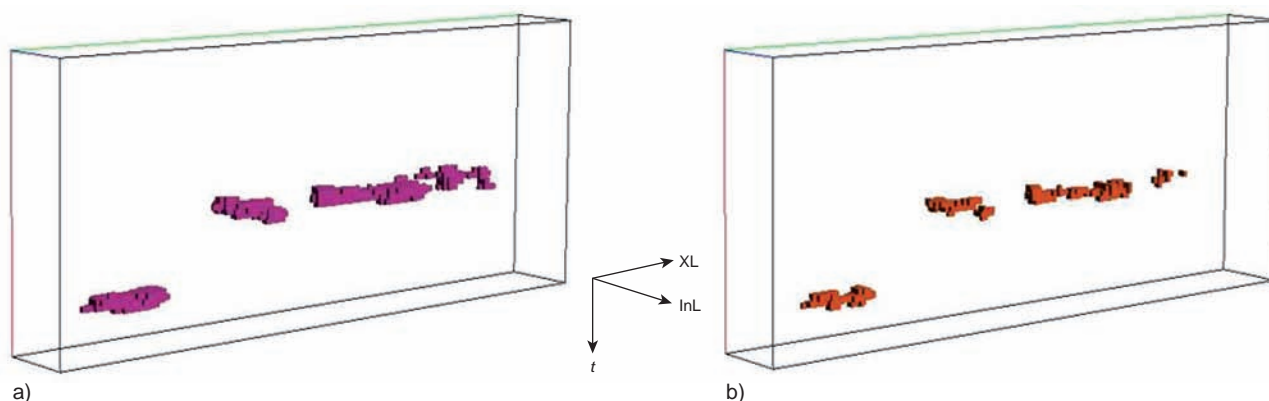


Figure 31

Geobody based on first principal component after 3 years of production computed on a) Noise-free seismic data, b) Noisy seismic data. Cube of 100 m in InL, 820 m in XL, from 225 ms to 275 ms.

stages, frequency filters between stages at peaks 115 and 57 Hz, RMS values of amplitude changes between stages, frequency filter between stages at peak 28 Hz, energy changes between stages. Keeping only values greater than 9.1 of this principal component provides the second geobody shown in Figure 30. This geobody corresponds to the very high steam saturation areas, and also to the higher values of temperature (greater than 179°C), higher values of mean effective stress, already partly produced areas (oil saturation 25% lower than over the whole reservoir). It is not efficient for detecting areas with steam saturations less than 50% (e.g. for the 1st month of production). Nevertheless, as observed from Figure 31, this geobody is stable to the noise which is of great interest if working on real seismic data. And moreover, this geobody proves the interest of the high seismic frequency content (in our case between 40 and 163 Hz, but mostly above 81 Hz) for delineating the very high steam saturation areas, and thus the potential of technologies such as permanent seismic acquisition as compared to traditional seismic acquisition.

## CONCLUSION

The purposes of the work presented here were, first, to better understand the links between heavy oil reservoir SAGD production and associated seismic amplitude changes along calendar time, second, to investigate permanent seismic acquisition interest for monitoring the steam chamber growth in heavy oil reservoirs. This work was done on a reservoir model of such a Canadian Athabasca reservoir (Hangingstone field). It involved seismic modelling followed by interpretation.

The ray+Born seismic modelling allowed us to create 4D seismic data corresponding to different stages of production

of the selected Canadian reservoir model. The pre-stack seismic data represent the *P*-wave response of the four elastic models at initial stage, at first month, sixth month and third year of production. The seismic amplitudes and the travel-times are correctly handled for the near and medium offsets.

The synthetic seismic data that we modelled were clean data as they did not contain any multiple, converted or refracted events. We were able to obtain a large seismic fold order for a binning of five by five square meters because the acquisition pattern was dense. So, we were in an ideal case for the post-processing. We performed a time migration on stacked data which allowed us to image the *V*-shaped steam chamber development and to observe time-shifts in the reservoir zone. In this way, we could follow the evolution of the reservoir over time. In order to obtain more realistic seismic data, random noise was added to the pre-stack data. The same post-processing workflow as for noise-free data was applied on noisy data. The migrated sections were then of lower quality, some reflectors being biased. Nevertheless, the time and amplitude differences between the four stages of production partially appeared.

Other processing tests could be performed on these synthetic data. For example, we could take into account a sparser acquisition and study its impact on migrated sections. What could also be done is to estimate the RMS velocity in a blind context. Some other migration techniques such as 3D time migration or depth migration could be tested, as well as azimuth trace sorting. The analysis of amplitude *versus* offset or incidence angle could allow us to estimate the ratio of *P*-velocity and *S*-velocity which is a useful parameter for interpretation.

Moreover, full-wave seismic modelling should be useful to study *S*-wave parameters (steam effect?), as well as visco-elastic

seismic modelling to study attenuation (heavy oil effect? weathered zone?).

Based on the 4D modelled seismic data (noise-free or noisy), some interpretation aspects were studied in order to provide guidelines for real cases. A first look at the seismic data showed that the geometry and volume of the steam zone cannot be clearly delineated even on noise-free seismic data, thus calling for enhanced interpretation methods. Moreover, the impact of the noise appeared very strong at all stages: this real noise completely overrides the seismic changes at the beginning of production.

A few seismic attributes like energy, frequency filters etc. were then studied. Some of these seismic attributes appear visually/qualitatively related to the lithofacies, but more importantly to the geomechanical/production properties. When working on real seismic data, one would better use 3D attributes like energy or energy changes between stages, or 2D attributes like maps of time differences between stages at reservoir top/bottom, since these seismic attributes are more robust to seismic noise. In future works, others seismic attributes should be evaluated, like amplitude envelop, instantaneous frequencies/phases, spectral components, or 3D cubes of time differences between stages that could maybe help for delineating heterogeneities in the reservoir.

Even if visual links were found out between these seismic attributes and geomechanical/production properties, no quantitative relationship could be defined: this confirms the need for PetroElastic or Rock Physics Modelling in 4D seismic data interpretation of heavy oil reservoirs produced with SAGD.

However, based on the seismic attributes, two geobodies were proposed. The second one, which is stable to the noise, corresponds to the very high steam saturation areas. And as this geobody accounts for high seismic frequencies in its construction (in our case between 40 and 163 Hz, but mostly above 81 Hz), it proves the potential of technologies providing high frequency contents for monitoring the steam chamber growth in heavy oil reservoirs, as compared to a traditional seismic acquisition of much lower frequency content. The next step would be now to confirm all these results on real 4D seismic data.

## ACKNOWLEDGMENTS

The results presented in this paper are part of a collaborative work between IFP Energies nouvelles and CGGVeritas, on SAGD recovery process in heavy oil unconsolidated sandstone reservoirs and its impact on seismic response.

The authors would like to thank IFP Energies nouvelles and CGGVeritas for permission to present this paper. The reviewers are also acknowledged for helping improving it.

## REFERENCES

- 1 Schmitt D.R. (1999) Seismic attributes for monitoring of a shallow heated heavy oil reservoir: A case study, *Geophysics* **64**, 2, 368-377. DOI: 10.1190/1.1444541.
- 2 Li G., Purdue G., Weber S., Couzens R. (2001) Effective processing of nonrepeatable 4-D seismic data to monitor heavy oil SAGD steam flood at East Senlac, Saskatchewan, Canada, *Lead. Edge* **20**, 1, 54-62. DOI: 10.1190/1.1438878.
- 3 Jenkins S.D., Waite M.W., Bee M.F. (1997) Time-lapse monitoring of the Duri steamflood: A pilot and case study, *Lead. Edge* **16**, 9, 1267-1273.
- 4 Bianco E. (2008) Seismic rock physics of steam injection in bituminous oil sand reservoirs, *Master of Science Thesis*, University of Alberta. ISBN: 978-0-494-47182-1.
- 5 Nakayama T., Takahashi A., Skinner L., Kato A. (2008) Oil sands reservoir monitoring using time-lapse 3D seismic in Canada, *International Petroleum Technology Conference*, Kuala Lumpur, Malaysia, 3-5 December, No. 12333.
- 6 Zhang W., Youn S., Doan Q. (2005) Understanding Reservoir Architectures and Steam Chamber Growth at Christina Lake, Alberta, by Using 4D Seismic and Crosswell Seismic Imaging, *SPE International Thermal Operations and Heavy Oil Symposium*, Calgary, Canada, 1-3 November, No. 97808. DOI: 10.2118/97808-PA.
- 7 Lerat O., Adjemian F., Baroni A., Etienne G., Renard G., Bathellier E., Forgues E., Aubin F., Euzen T. (2010) Modelling of 4D Seismic Data for the Monitoring of Steam Chamber Growth During the SAGD Process, *J. Can. Petrol. Technol.* **49**, 6, 21-30. DOI: 10.2118/138401-PA.
- 8 Beydoun W.B., Mendes M. (1989) Elastic Ray-Born  $L_2$ -Migration/Inversion, *Geophys. J. Int.* **97**, 1, 151-160. DOI: 10.1111/j.1365-246X.1989.tb00490.x.
- 9 Thierry P., Operto S., Lambaré G. (1999) Fast 2D ray-Born migration/inversion in complex media, *Geophysics* **64**, 1, 162-181.
- 10 Lambaré G., Operto S., Podvin P., Thierry P. (2003) 3D ray+Born migration/inversion – Part 1: Theory, *Geophysics* **68**, 4, 1348-1356. DOI: 10.1190/1.598128.
- 11 Ciz R., Shapiro S.A. (2007) Generalization of Gassmann equations for porous media saturated with a solid material, *Geophysics* **72**, 6, A75-A79. DOI: 10.1190/1.2772400.
- 12 Beylkin G., Burrigge R. (1990) Linearized inverse scattering problems in acoustic and elasticity, *Wave Motion* **12**, 15-52, North-Holland.
- 13 Nicolétis L., Svay-Lucas J., Clochard V., Compte P. (1997) 3D true-amplitude migration of 3C compressional and converted shear waves, *J. Seism. Explor.* **6**, 127-142.
- 14 Wu R.S. (1989) The Perturbation Method in Elastic Wave Scattering, *Pure Appl. Geophys.* **131**, 4, 605-637. DOI: 10.1007/BF00876266.
- 15 Macé D., Bourgeois A., Etienne G., Richard V. (1994) 2D linearized elastic inversion - Evaluation on synthetic data, *Modeling the Earth for Oil Exploration*, Helbig K. (ed.), Final report of the CEC's - Geoscience 1, Pergamon Press, pp. 589-615.
- 16 Rickett J., Biondi B., Lumley D. (1997) Modeling heterogeneous reservoirs using the first order Born approximation, *Stanford Exploration Project* **92**, 79-86.

- 17 Rousseau V., Nicolétis L., Svay-Lucas J., Rakotoarisoa H. (2000) 3D true amplitude migration by regularization in the angle domain, *62nd EAGE Conference & Exhibition*, Glasgow, England, 29 May-02 June.
- 18 Beylkin G., Oristaglio M., Miller D. (1985) Spatial resolution of migration algorithms, in *Acoustical Imaging, Vol. 14*, Berkhout A.J., Ridder J., Van der Waal L.F. (eds), Plenum Pub. Co, pp. 155-167. ISBN: 978-0-306-42094-8.
- 19 Malin P.E., Phinney R.A. (1985) On the relative scattering of *P*- and *S*-waves, *Geophys. J. Int.* **80**, 3, 603-618. DOI: 10.1111/j.1365-246X.1985.tb05113.x.
- 20 Chopra S., Marfurt K. (2007) Seismic attributes for prospect identification and reservoir characterization, *SEG Geophysical Developments Series*, No. 11. ISBN: 1-56080-141-7.
- 21 Cooley W.W., Lohnes P.R. (1971) *Multivariate data analysis*, John Wiley & Sons Inc., New York. ISBN: 0471170607, 9780471170600.

*Final manuscript received in October 2011  
Published online in March 2012*

Copyright © 2012 IFP Energies nouvelles

Permission to make digital or hard copies of part or all of this work for personal or classroom use is granted without fee provided that copies are not made or distributed for profit or commercial advantage and that copies bear this notice and the full citation on the first page. Copyrights for components of this work owned by others than IFP Energies nouvelles must be honored. Abstracting with credit is permitted. To copy otherwise, to republish, to post on servers, or to redistribute to lists, requires prior specific permission and/or a fee: Request permission from Information Mission, IFP Energies nouvelles, fax. +33 1 47 52 70 96, or [revueogst@ifpen.fr](mailto:revueogst@ifpen.fr).